Diverse Origins of Gases From Mud Volcanoes and Seeps in Tectonically Fragmented Terrane

Yueh-ting Lin, Douglas Rumble, Edward Young, Jabrane Labidi, Tzu-hsuan Tu, Jhen-nien Chen, Thomas Pape, Gerhard Bohrmann, Saulwood Lin, Li-hung Lin, et al.

Diverse origins of gases from mud volcanoes and seeps in tectonically fragmented terrane

Yueh-Ting Lin[1], Douglas Rumble[2], Edward D. Young[3], Jabrane Labidi[3,4], Tzu-Hsuan Tu[1,5], Jhen-Nien Chen[1], Thomas Pape[6], Gerhard Bohrmann[6], Saulwood Lin[7], Li-Hung Lin[1,8*], and Pei-Ling Wang[7,8*]

[1]Department of Geosciences, National Taiwan University, Taipei 106, Taiwan
[2]Geophysical Laboratory, Carnegie Institution for Science, Washington DC 20015, USA
[3]Department of Earth, Planetary and Space Sciences, University of California Los Angeles, Los Angeles, CA 90095, USA
[4]Université de Paris Cité, Institut de Physique du Globe de Paris, CNRS, F-75005 Paris, France
[5]Department of Oceanography, National Sun Yat-sen University, Kaohsiung 804, Taiwan
[6]MARUM – Center for Marine Environmental Sciences and Faculty of Geosciences, University of Bremen, 28359 Bremen, Germany
[7]Institute of Oceanography, National Taiwan University, Taipei 106, Taiwan
[8]Research Center for Future Earth, National Taiwan University, Taipei 106, Taiwan

*Correspondence at:
Li-Hung Lin
Department of Geosciences, National Taiwan University, Taipei 106, Taiwan
Email: lhlin@ntu.edu.tw

and

Pei-Ling Wang
Institute of Oceanography, National Taiwan University, Taipei 106, Taiwan
Email: plwang@ntu.edu.tw

Key point:

- Mud volcanoes and gas seeps provide a rapid access to probing subsurface fluid characteristics in tectonically active regions.
- Thermogenic methane constitutes a major component of hydrocarbons and forms at temperatures of 99-260°C.
- A wide spectrum of geochemical characteristics indicates diverse formation mechanisms and conditions that constrain gas and water origins.

Abstract

Identification of methane origins remains a challenging work as current diagnostic signals are often not sufficient to resolve individual formation and post-formation processes. To address such a knowledge gap in a tectonically active and fragmented terrain, samples from mud volcanoes, gas seeps, and springs distributed along structural features onshore and offshore of Taiwan were analyzed for their isotopic compositions of methane, nitrogen, helium, dissolved inorganic carbon, CO_2, and water. Our analyses yielded $\Delta^{13}CH_3D$ and $\Delta^{12}CH_2D_2$ values ranging between +1.9‰ and +7.8‰, and between +3.0‰ and +19.9‰, respectively. A portion of the samples were characterized by values that represent the thermodynamic equilibrium at temperatures of 99–260°C. These temperature estimates, together with the bulk isotopic compositions and local geothermal gradients (25-30^{o}C/km), suggest that methane was formed by thermal maturation of organic matter at depths of 2 to 9 km below the land surface and channeled upward along faults. Other samples were found to deviate from equilibrium by varying degrees. Considering the geological background, helium isotopic ratios, and nitrogen isotopologue compositions, and methanogens detected at some sites, these gases are either abiotic in origin or a mixture of microbial and thermogenic sources. Regardless of whether the equilibrium of methane isotopologues was reached, few sites hosted by sedimentary formations were characterized by mantle-like helium signatures, indicating decoupled origins and potential degassing of helium from the relic igneous source. Overall, these results suggest the extraction of methane and other gases from multiple depths from strata fragmented by fault displacement in an active orogenic belt.

Plain Language Summary

Mud volcanoes and gas seeps are distributed primarily in active tectonic regimes

and represent the surface expression of subsurface fracture networks. They provide rapid access to probing subsurface characteristics for the generations of methane, other gases, and water. Identifying the exact mechanisms of methane formation remains a challenging work due to the lack of diagnostic signals with sufficient resolving power. This study employed a wide range of isotopic tools to constrain the origins of gases and water from mud volcanoes and seeps in Taiwan, where dual subductions and associated arc-continent collision between the Philippine Sea and Eurasian plates have enabled the plumbing of gases and water in accordance with structure development and stratum deformation. Our results reveal a spectrum of geochemical characteristics that point to diverse formation mechanisms and conditions. In particular, deeply sourced thermogenic methane (from depths of 2 to 9 km) appears to constitute a major gas component at most sites, and is mixed by various degrees with abiotic methane pertinent to igneous bodies emplaced during subduction/collision, or microbial methane generated at shallow depths. Overall, the results address the temporal and spatial variations in gas origins prone to terrain fragmentation and dynamic structural control associated with mountain building.

Keywords:

methane isotopologue, helium isotope, mud volcano, seep, active tectonic regime

1. Introduction

Methane is the main gas component associated with petroleum and coal systems (Lundegard et al., 2000). Three major mechanisms have been suggested for its formation, including biological production from CO_2 and methylated compounds, stepwise thermal degradation of complex organic matters, and to a lesser extent, the Fischer-Tropsch Type reaction catalyzed by metals or sulfide minerals (Kietäväinen & Purkamo, 2015; Schoell, 1988; Stolper et al., 2014). Identifying the exact mechanisms and quantifying their fluxes from individual sources would greatly enhance our understanding of carbon cycling between reservoirs and their impact on future climate.

Mud volcanoes and seeps represent the surface expression of subsurface fracture networks and are considered to be an effective channel of methane emission (Kopf, 2003; Etiope, 2009). Gases (predominantly hydrocarbons), water, and unconsolidated sediments originating from deep environments migrate upward due to gravitational instability and overpressurization driven by rapid burial and fault displacement (Carson & Screaton, 1998), facilitating the minimum alteration of gas during channel transport, and the direct methane emissions into the atmosphere or seawater. Therefore, the geochemical characteristics of methane (e.g., abundance and isotopic composition) could potentially serve as an indicator of methane formation conditions, and the connectivity and extent of fractures in the crustal plumbing system (Mazzini & Etiope, 2017; Milkov & Etiope, 2018).

Methane isotopic compositions ($^{13}C/^{12}C$ and $^{2}H/^{1}H$) and abundance ratios as compared to higher hydrocarbons (C_1/C_2^+) are conventionally used to characterize methane origins (e.g., Bernard et al., 1977; Whiticar, 1999). The principle stems from experimental and field observations that constrain various degrees of isotopic fractionations and abundance ratios for different methane-formation mechanisms (Milkov and Etiope, 2018). These fingerprints are not unequivocal, as they are subject to further alteration caused by secondary processes, such as mixing, migration, and microbial oxidation (e.g., Bernard et al., 1977; Whiticar, 1999). The advancement of mass spectrometric techniques has enabled the measurement of two doubly substituted isotopologues ($^{13}CH_3D$ and $^{12}CH_2D_2$) at high precision (Young et al., 2016). The isotopologue approach provides a direct means to assess whether the methane has reached isotopic equilibrium (with coherent temperature estimates from

two thermometers), overcoming the potential bias derived from the abundance of single doubly substituted isotopologue quantified by either mass or optic spectroscopy (Douglas et al., 2017; Ono et al., 2014; Young et al., 2016). Furthermore, the approach adds two additional constraints to conventional mixing models based on mass conservation, thereby facilitating coherent reservoir or process mixing models among different isotopic signals and better identification of end components. Finally, gas origins could best be resolved with additional isotopic fingerprints of the constituent gases. While helium isotope ratios are conventionally exploited to differentiate mantle from crust and atmospheric sources (Poreda & Craig, 1989), the abundances of rare nitrogen isotopologues emerge as a sensitive indicator to track the cycling of air-derived nitrogen that could be falsely identified as the mantle nitrogen using the bulk nitrogen isotopic compositions (Labidi and Young, 2022). The approaches arise from the observation that mantle derived $^{15}N^{15}N$ abundances (from mid-ocean ridges and plumes) are consistent with the stochastic distribution for the intramolecular equilibrium, and are greatly distinctive from atmospheric nitrogen (Labidi et al., 2020). These results combined with bulk nitrogen isotopic compositions and noble gas ratios enable to trace nitrogen cycling associated with subduction and hydrothermal circulation potentially impacted by air contamination, as well as to identify the primordial mantle (Labidi et al., 2020 and 2021; Labidi and Young, 2022). As terranes associated with subduction systems are fragmented by faulting and magmatism, gases that originate from multiple sources likely have distinctive combined isotopic patterns. The integration of multiple isotopic fingerprints (bulk and isotopologue) for specific geological occurrences offers insights into gas formation, mixing, and alteration that have rarely been explored.

This study aims to determine the origins of methane from mud volcanoes and seeps onshore and offshore Taiwan by combining the abundances of rare methane and nitrogen isotopologues, and bulk isotopic compositions of helium, methane, dissolved inorganic carbon (DIC), CO_2, and water. The study materials were chosen to take advantage of Taiwan's unique tectonic setting, at the intersection of dual subduction systems between the Eurasian and Philippine Sea plates (Lallemand, 2016). Mud volcanoes/seeps are associated with different structural features in different geological units, providing ideal opportunities to probe gas reservoirs in fragmented subsurface environments. These isotopic results were integrated with

158 geological characteristics to address mechanisms and potential depths of methane
159 formation, and post-formation mixing and alteration.
160
161 2. Site background
162 Taiwan is located in an active tectonic setting, at the boundary between the
163 Philippine Sea plate and the Eurasian plate (Suppe, 1984; Teng & Lin, 2004). Major
164 structures are oriented roughly northeast-southwest as a result of compression driven
165 by the convergence and collision between the Luzon arc and the Eurasian continent.
166 Geological units on land, from west to east, include the Coastal Plain, the Western
167 Foothills, the Hsuehshan Range, the Central Range (Backbone Range), the
168 Longitudinal Valley, and the Coastal Range (Teng & Lin, 2004). A developing
169 accretionary wedge is located offshore of southwestern Taiwan and features ridges
170 and pockmarks (bathymetric depressions often interpreted as the signature of
171 subseafloor fluid transport) that have been postulated to extend from corresponding
172 structures on land (Figure S1; Liu et al., 1997). Seismic surveys across the transect
173 between Taiwan and the Eurasian continent reveal two structural domains (active and
174 passive continental margins) separated by a projected deformation front that
175 represents the extension of the Manila Trench (Lin et al., 2008). The active margin is
176 further composed of the Upper Slope unit to the east, where mud diapirs predominate,
177 and the Lower Slope unit to the west, where anticlinal ridges have formed (Chen et
178 al., 2014; Wang et al., 2022). Numerous mud volcanoes and seeps are distributed
179 along faults or near anticlinal axes in southwestern and eastern Taiwan, and offshore
180 southwestern Taiwan (Chao et al., 2011; Chen et al., 2017; Sun et al., 2010). Field
181 sites investigated here are distributed near, or along structures, including the Chukou
182 fault, Chishan fault, Gutingkeng anticline, blind structures in the Coastal Plain,
183 Longitudinal Valley fault, volcanic complexes, and the Formosa and Four Way
184 Closure ridges offshore southwestern Taiwan (Figure S1; Table S1). A more detailed
185 description of the site background is given in the Supporting information.
186
187 3. Materials and methods
188 3.1 Field sampling and sample processing
189 A total of 31 gas and water samples were collected from 23 mud volcanoes, gas
190 seeps, and boreholes (Table S1). For most samples, gases were collected directly

from bubbling features with the most vigorous activity. Sites AT and YSES are boreholes connected with a gas-water separator. Site GI-03 was an artisan well with vigorous bubbling, whereas site GI-01 was a pond (episodically flooded with seawater) with several bubbling features. To perform sampling at most sites, gases were drained into 50 mL gas-tight, pre-evacuated glass bottles with two stopcocks connected to a funnel. The funnel was first placed above bubbling features and filled with water. Water in the funnel was replaced gradually with the exsolved gases. The gases were used to purge the connecting tubing five times, and drained into pre-evacuated glass bottles (Figure S2). Sampling procedures were adjusted for three sites (YSES, WD, and AT). For samples from sites YSES and AT, gases discharged from the gas-water separator were directly diverted into pre-evacuated glass bottles. For samples from site WD, high erupting activities and outflowing water temperatures (63°C) prohibited direct sampling access. Therefore, mud and water flowing to the rim of the affected area were drained into serum bottles without headspace and capped with blue butyl rubber stoppers. Gases were extracted by connecting the sample bottles with pre-evacuated glass bottles. A total of five replicate bottles were collected for multiple gas analyses.

Offshore gas samples were collected from sediment cores drilled into gas-hydrate bearing zones at Formosa Ridge (site FR) and Four Way Closure Ridge (site FWCR) with the seafloor drill rig MARUM-MeBo200 during cruise SO266 with *R/V SONNE* (Bohrmann et al., 2023). Sediment cores dedicated to gas sampling were collected with pressure core samplers (Pape et al., 2017) and kept under in situ pressure during core retrieval. During onboard gas sampling, the pressure core was first depressurized slowly while monitoring gas pressure. Gases were collected into stainless steel cylinders when the incremental gas pressure increased abruptly (up to 725 psi), an indicator of hydrate dissociation.

For all sites, water temperatures were measured on-site. Water samples were collected in 50 mL tubes and centrifuged at a speed of 10,000 ×g for 20 min. The supernatant was filtered through 0.22 μm pore-sized cellulose membranes and stored with no headspace at room temperature.

3.2 Sample analyses

CH_4, C_2H_6, C_3H_8, and CO_2 concentrations were analyzed by a gas

chromatograph (GC; 6890N, Agilent Technologies) with a flame ionization detector, and a thermal conductivity detector in line with a Porapak Q column using helium as the carrier gas. DIC concentrations were analyzed on CO_2 gases exsolved from water acidified with phosphoric acid (5%) using a CO_2 analyzer (Aurora 1030, O.I. Analytical). The reported gas abundances were corrected for the air assuming that oxygen measured was derived from the air and the N_2/O_2 ratio is 3.7. Since all samples were collected in 5 replicates, the sample was discarded if the air constituted the main component of the gases.

Carbon isotopic compositions of CH_4, DIC and CO_2 were measured with a MAT253 isotope ratio mass spectrometer (IRMS) equipped with a GC IsoLink (Thermo Fisher Scientific) hosted at the National Taiwan University. The isotopic compositions are expressed in δ notation using the following equation:

$$\delta^{13}C = (R_{sample} / R_{standard} - 1) \times 1000‰ \quad \text{eq. 1}$$

where R is $^{13}C/^{12}C$, and the standard is Vienna Pee Dee Belemnite (VPDB).

For noble gas analyses, gases were introduced into a preline system for purification and separation. Helium isotopic ratios ($^3He/^4He$) and neon concentrations were measured by a helium isotope mass spectrometer (Helix, Thermo Scientific) in line with a quadrupole mass spectrometer (QMS200, Pfeiffer Vacuum). Helium ratios were calibrated against the standard atmospheric helium (Mishima et al., 2018) and a standard with a $^3He/^4He$ ratio 20.4 times of the atmospheric ratio (R_a) provided by the University of Tokyo (Sano et al., 2008), whereas neon concentrations and He/Ne ratios were calibrated against the air. Helium isotope ratios are expressed relative to the air using the following equation:

$$R/R_a = (^3He/^4He)_{sample} / (^3He/^4He)_{atmosphere} \quad \text{eq.2}$$

where R and R_a are the $^3He/^4He$ ratios of sample and atmospheric helium, respectively.

Hydrogen and oxygen isotope compositions of water were measured by an Off-Axis Integrated Cavity Output Spectrometer (Los Gatos Research). The isotopic compositions are expressed in δ notation (eq. 1) with reference to VSMOW (Vienna

Standard Mean Ocean Water).

Typical analytical uncertainties were 5% for gas concentrations, 2% for DIC concentrations, 0.2‰ for $\delta^{13}C$ values, 0.2‰ for $\delta^{18}O_{H2O}$ values, 1.0‰ for $\delta^{2}H_{H2O}$ values, and 2% for $^{3}He/^{4}He$. The detection limits for gas abundances and DIC concentrations were 10 ppmv, and 0.05 mM, respectively.

For methane isotopologues, currents of $^{12}CH_4^+$, $^{13}CH_4^+$, $^{12}CH_3D^+$, $^{13}CH_3D^+$, and $^{12}CH_2D_2^+$ were measured using the Panorama (Nu Instruments) at the University of California at Los Angeles following established protocols (Giunta et al., 2019; Young et al., 2016, 2017). The mass resolving power of the spectrometer was equal to, or greater than 40,000, allowing for the resolution of two mass-18 isotopologues, $^{13}CH_3D$ and $^{12}CH_2D_2$. Methane was purified using a GC equipped with two packed columns filled with 5A molecular sieve and HayeSepD porous polymer using helium as the carrier gas. Purified methane was collected, transferred, and expanded into the sample bellows connected to the mass spectrometer. In general, $^{12}CH_3D^+/^{12}CH_4^+$ and $^{12}CH_2D_2/^{12}CH_4^+$ ratios, and $^{13}CH_4^+/^{12}CH_4^+$ and $^{13}CH_3D/^{12}CH_4^+$ ratios were measured with more than twenty blocks of data acquisition. In each block, alternating measurements on 20 samples and 21 standards were cycled every 30 seconds. Data was further integrated over individual blocks. The bulk isotopic compositions are adopted from $^{13}CH_4^+/^{12}CH_4^+$ and $^{12}CH_3D^+/^{12}CH_4^+$, and expressed in δ notation ($\delta^{13}C$ and $\delta^{2}H$ referenced to VPDB and VSMOW, respectively; eq. 1), whereas the isotopologue abundances are shown as uppercase delta values, defined as:

$$\Delta^{13}CH_3D = [(^{13}CH_3D/^{12}CH_4)_{sample}/ (^{13}CH_3D/^{12}CH_4)_{stochastic} - 1] \times 1000‰ \quad \text{eq. 3}$$

$$\Delta^{12}CH_2D_2 = [(^{12}CH_2D_2/^{12}CH_4)_{sample}/ (^{12}CH_2D_2/^{12}CH_4)_{stochastic} - 1] \times 1000‰ \quad \text{eq. 4}$$

where the ratio of the isotopologues under stochastic conditions was calculated using the bulk isotope composition. Typical internal uncertainties for $\Delta^{13}CH_3D$, and $\Delta^{12}CH_2D_2$ values were less than ±0.2‰ and ±0.6‰ 1σ, respectively (Young et al., 2016, 2017).

The equilibrium temperatures were calculated following the relationship described in Young et al. (2016 and 2017):

$$\Delta^{13}CH3D \approx 1000 \times \ln (1 + 0.0355502/ T\text{-}433.038/ T^2 + 1270210.0/ T^3 \text{-}5.94804 \times 10^8/$$

$T^4 + 1.196630 \times 10^{11}/ T^5 - 9.0723 \times 10^{12}/ T^6)$ eq. 5

$\Delta^{12}CH_2D_2 \approx 1000 \times \ln (1 + 0.183798/ T - 785.483/ T^2 + 1056280.0/ T^3 + 9.37307 \times 10^7/ T^4 - 8.919480 \times 10^{10}/ T^5 + 9.901730 \times 10^{12}/ T^6)$ eq. 6

where T is in Kelvin.

Nitrogen isotopologues for five samples (sites KTL-02, WSD-01, AT, GI-01, and GI-03) were also determined. In short, nitrogen was purified on the same preline system as methane (Young et al., 2016). The abundances of $^{14}N^{14}N^+$, $^{14}N^{15}N^+$, and $^{15}N^{15}N^+$ ions were measured at a mass resolving power of approximately 50,000 (Labidi & Young, 2022). Data are expressed as $\delta^{15}N$ (eq. 1; referenced to the air) and Δ_{30} (Yeung et al., 2017):

$\Delta_{30} = (^{30}R/ (^{15}R)^2 - 1) \times 1000‰$ eq. 7

where $^{30}R = {}^{15}N^{15}N/ {}^{14}N^{14}N$ and $^{15}R = {}^{15}N/ {}^{14}N$.

4. Results

Gas compositions and isotopic compositions are shown in Figure 1 and Table S1. Gases in most samples were dominated by methane (>75%), with the exception of CO_2-rich (>80%) gases from sites CLS and CLP (Table S1). Minor amounts of ethane (0.1-1.7%) and propane (0-0.4%) were observed in all samples. Bulk carbon and hydrogen isotopic compositions of methane spanned over a wide range ($\delta^{13}C_{CH4}$ from -86.9‰ to -16.7‰ and δ^2H_{CH4} from -206.4‰ to -78.4‰) with the majority of $\delta^{13}C_{CH4}$ and δ^2H_{CH4} values clustering between -39.3‰ and -30.7‰ and between -167.8‰ and -138.5‰, respectively. While DIC $\delta^{13}C$ values were from -29.5‰ to +30.6‰, DIC concentrations varied considerably between 0.4 mM and 271.3 mM. For comparison, $\delta^{13}C_{CO2}$ values ranged from -24.8‰ to +20.5‰.

The $\Delta^{13}CH_3D$ and $\Delta^{12}CH_2D_2$ values ranged between +1.90‰ and +7.83‰ and between +2.97‰ and +19.85‰, respectively (Figure 2; Table S2). Among all samples, eight (CLP, CLS, KTL, SYNH-02, WSD-01, WD, AT, and LS) had isotopologue abundances consistent with the thermodynamic equilibrium at temperatures ranging from 23°C to 260°C (Table S2). Other samples were

characterized. by values deviating from the equilibrium by varying degrees (Figure 2). The $\delta^{15}N$ and Δ_{30} values ranged between -2.1‰ and +3.6‰, and between 1.8‰ and 16.4‰ relative to the stochastic distribution of isotopologues, respectively (Figure S3; Table S3).

Helium isotopic compositions spanned from 0.1 to 5.4 Ra. Eight samples possessed $^{3}He/^{4}He$ ratios of >1 Ra (Figure 3; Table S4). The $\delta^{2}H_{H20}$ and $\delta^{18}O_{H20}$ values spanned from -52.5‰ to -1.0‰, and from -8.1‰ to +6.4‰, respectively (Figure 4a; Table S5). While eight samples from the Chukuo fault and Coastal Range fell along the local meteoric water line (LMWL; Peng et al., 2010), the others deviated from the LMWL by varying degrees.

5. Discussion

5.1 First order assessments on the origins of methane

Conventional approaches based on bulk isotopic compositions of methane and CO_2, and abundance ratios were first used to interpret the origins of hydrocarbon gases for individual structural domains (e.g., Milkov, 2011; Milkov & Etiope, 2018). The principle stems from laboratory and field observations (e.g., Bernard et al., 1977; Whiticar, 1999; Milkov & Etiope, 2018) that thermogenic gases are generally characterized by relatively high $\delta^{13}C_{CH4}$ and $\delta^{2}H_{CH4}$ values (from -60‰ to -25‰, and -300‰ to -150‰, respectively), low C_1/C_2^+ ratios (1 to 100), and low $\delta^{13}C_{CO2}$ values. Microbial gases possess geochemical characteristics (low $\delta^{13}C_{CH4}$ and $\delta^{2}H_{CH4}$ values (< -50‰ and <-150‰, respectively; Whiticar, 1999), and high C_1/C_2^+ ratios (>1000; Bernard et al., 1977)) distinct from thermogenic gases by various degrees (even though the less fractionated isotopic compositions of microbial methane resemble early mature thermogenic gases). Abiotic gases may follow variable patterns partially overlapping with thermogenic gases and with a tendency toward greater $\delta^{13}C_{CH4}$ values (Milkov & Etiope, 2018). For comparison, as CO_2 derived from biodegraded oil is converted into secondary microbial methane, the residual CO_2 becomes progressively enriched in ^{13}C (Head et al., 2003). Biodegradation also leads to an increasing CH_4 fraction in the gas. Furthermore, methane oxidation (aerobic and anaerobic styles) and diffusive transport would all lead to the residue methane enriched with ^{13}C and ^{2}H by various degrees (Figure 1; Whiticar, 1999). Therefore, gas alteration and mixing can complicate possible interpretations.

Based on these empirical fields defined in $\delta^{13}C$ and $\delta^{2}H$ values, and C_1/C_2^+ ratios, 15 out of the 31 samples could be interpreted as dominantly thermogenic in origin (Figure 1; Table S1; S2). While these samples were primarily distributed along the Chukou and Chishan faults, 4 of the 15 were from the Coastal Range (sites LGH and LS), the Gutingkeng anticline (site LCW), and the Coastal Plain (site WD). For comparison, data for two boreholes from the Coastal Range (sites AT and GI) were interpreted as abiotic in origin (Figure 1). On the Bernard plot (Figure 1b), these data points fell either within the empirically defined abiotic field or the overlapping range between the thermogenic and abiotic fields (Milkov and Etiope, 2018). The $\delta^{2}H_{CH4}$ values for both sites (between -79‰ and -77‰) and the $\delta^{13}C_{CH4}$ value for site GI were much higher than those commonly identified as thermogenic methane. This, combined with their high temperature nature, proximity to the volcanic bodies, and island arc setting suggest that methane could be abiotic (Milkov, 2011; Milkov and Etiope, 2018). Data for two marine sediments (sites FR and FWCR) were categorized as microbial in origin, whereas data points for LGH (Coastal Range), TDS (Coastal Plain), YSES (Chukou fault), and all samples from the Gutingkeng anticline fell between typical ranges of thermogenic and microbial end components (Figure 1b; see section 5.3 for the mixing model).

The $\delta^{13}C_{CO2}$ values of samples collected from the Chishan fault fell between -15.9‰ and +20.5‰ (Figure 1c; Table S1). In particular, $\delta^{13}C$ values of CO_2 and DIC for SYNH-01, and WSD -01 and -02 ranged from +8.9‰ to +20.5‰ and from +18.5‰ to +30.6‰, respectively. This, combined with the detection of active CO_2 reducing methanogens in the region (Cheng et al., 2012; Lin et al., 2018) suggests that the ^{13}C enrichment in CO_2 is catalyzed by secondary methane formation from CO_2. Secondary microbial methane is formed through the anaerobic degradation of petroleum (Head et al., 2003). As CO_2 is the byproduct of petroleum degradation, its quantity is limited by the degradability of petroleum, and therefore, considered as the close system. In this regard, further methane formation would preferentially reduce $^{12}CO_2$ over $^{13}CO_2$, leaving the residue CO_2 enriched with ^{13}C and methane depleted in ^{13}C. The interpretation is also supported by the presence of patchy oils constantly observed in the bubbling pools or craters. To assess this process, a Rayleigh distillation model was applied assuming an initial $\delta^{13}C_{DIC}$ value of -25‰ and a fractionation factor (αDIC-CH_4) of 1.05 (Chasar et al., 2000). The calculation also

assumed that CO_2 or DIC in environments was produced primarily from the degradation of organic matter with $\delta^{13}C$ values between -30‰ and -20‰ (Campeau et al., 2017). Since the isotopic fractionation for organic degradation is small (<1‰), the median $\delta^{13}C$ value (-25‰) was arbitrarily chosen for modeling. The calculation suggests that in order to replicate the observed $\delta^{13}C_{DIC}$ value, the fraction of reaction would be 36% or the concentration of DIC consumed or methane produced would be equivalent to 57 mM. The quantity of DIC reduced or methane produced is at least one order of magnitude higher than the observed maximum methane concentration (2 mM). If the fractionation factor is raised to a more extreme level of 1.08 (Summons et al., 1998), the reaction fraction would reach 54%, or the concentration of methane produced would be 34 mM. The overall results from the Rayleigh distillation modeling suggest that secondary methane formation by CO_2 reducing methanogens might not be solely responsible for the ^{13}C enrichment in CO_2 or DIC. Other microbial channels, such as acetate formation from CO_2 (Karakashev et al., 2006), might be involved. Alternatively, the high predicted concentration of methane could have been lost due to the depressurized degassing during transport along the fluid conduit. The temperature of methane formation for SYNH has been estimated to be up to 236^{o}C (Figure 2; Table S2). By applying a local geothermal gradient of 25^{o}C/km (Chi & Reed, 2008), the formation depth could range up to 9 km below the land surface. As methane ascends toward the land surface, dissolved methane would be depressurized and transformed into bubbles. The inference is supported by vigorous bubbling at SYNH during sampling.

The excess methane or carbon could not be accounted for by the anabolic assimilation as most substrate consumptions are often diverted to the energy yield rather than biosynthesis. For example, tests on *S. funaroxidans* cocultured with *M. hungate* have obtained a yield of 0.15-0.25 mole-CH_4/g-dw-biomass (Scholten & Conard, 2000). If 50% of biomass is attributed to carbon, the yield would range from 3.57 to 5.95 mole-CH_4/mole-C-biomass. For every mole of CO_2 utilized, less than 20% of it is diverted to biomass generation. Even with this, the predicted CO_2 consumption or CH_4 production still greatly exceeds the observed methane concentrations. In sum, the bulk isotopic compositions provide a first-order interpretation for the origin of hydrocarbons (methane in particular). While the excess methane predicted for the Chishan fault could have been accounted for by the

depressurization loss, the interpretation for the origins of all samples is still subject to variations caused by potential mixing with a small fraction of non-major end components.

The majority of $\Delta^{13}CH_3D$ and $\Delta^{12}CH_2D_2$ values for samples from the Chukou and Chishan faults, and the Coastal Range were distributed either on, or close to the equilibrium curve (Figure 2). The equilibrium temperatures were calculated to range from 23°C to 260°C for sites CLP, CLS, and KTL in the Chukou fault, sites WSD-01 and SYNH-02 in the Chishan fault, site WD in the Coastal Plain, and sites AT and LS in the Coastal Range (Table S2). Except for sites WSD-01 and AT, samples that displayed the isotopologue equilibrium also possessed bulk isotopic compositions and abundances interpreted as the products of thermal maturation of organic matters at high temperatures. Such a pattern is comparable with the observations of large-scale continental sedimentary basins, the Southwest Ontario and the Michigan Basin, as described in Giunta et al. (2019). Although the $\Delta^{13}CH_3D$ and $\Delta^{12}CH_2D_2$ values for sites WSD-01 and AT yielded comparable temperature estimates, these isotopologue abundances were considered to represent either a mixture of thermogenic and microbial (for site WSD-01) sources, or abiogenic methane (for site AT) (see sections 5.3 and 5.4).

5.2 Re-equilibration and other secondary processes for methane

Post-formation secondary mechanisms, including re-equilibration, microbial methane oxidation, and diffusive transport, have been proposed to explain the variations in clumped isotope composition that do not align well with the thermodynamic equilibrium (Beaudry et al., 2021; Giunta et al., 2021; Giunta et al., 2022; Jautzy et al., 2021; Krause et al., 2022; Labidi et al., 2020; Liu et al., 2023; Ono et al., 2021; Shuai et al., 2018; Stolper et al., 2015; Young et al., 2017). Re-equilibration is referred to the process that alters the original clumped isotopic compositions toward or along the thermodynamic equilibrium at a temperature range or condition either comparable with or drastically different from the current in situ setting. Because the re-equilibration takes place with intra-molecular re-ordering, the bulk isotopic compositions could have remained unaltered (Giunta et al., 2021; Labidi et al., 2020). The mechanism has been used to account for the origins of methane from the Precambrian continental shield, hydrothermal systems, Baltic Sea sediments, and

seep sediments from the Marmara Sea (Ash et al., 2019; Giunta et al., 2021; Labidi et al., 2020). The interpretation becomes even more appealing when the bulk isotopic compositions are apparently kinetic controlled (e.g., microbial methanogenesis) and clumped isotopic compositions reflects a state of or close to the thermodynamic equilibrium (Ash et al., 2019; Giunta et al., 2022; Ono et al., 2021).

To assess this inference, the probability of data distribution for $\Delta^{13}CH_3D$ and $\Delta^{12}CH_2D_2$ values for mud volcanoes in western Taiwan and offshore sediments were plotted considering their structural configuration and hosted formations might resemble each other (Figure S4). Like that reported by Giunta et al. (2021), the $\Delta^{13}CH_3D$ values were scattered across the measured range and did not exhibit any pattern that demonstrated the clustering within a particular interval. In contrast, the $\Delta^{12}CH_2D_2$ values clustered within two broad ranges (0-8‰ and 12-17‰) if a 1‰ interval was chosen. The bi-modal data distribution became even more prominent if a 2‰ interval was used (Figure S4). The re-equilibration hypothesis lies on the premise that the intra-molecular re-ordering of $^{12}CH_2D_2$ proceeds at a rate much faster (probably 2 times higher) than $^{13}CH_3D$. Therefore, over the course of re-equilibration, $\Delta^{13}CH_3D$ values produced by kinetic reactions (e.g., methanogenesis or thermal maturation) would vary toward the equilibrium line while $\Delta^{12}CH_2D_2$ values remain at a relatively invariant range. Under this circumstance, the estimated temperature projected by clustering $\Delta^{12}CH_2D_2$ values could be used to infer the possible temperature of re-equilibration, whereas $\Delta^{13}CH_3D$ values represent the degrees of partial re-equilibration. The inference of re-equilibration described above is not favored based on the following arguments.

(1) The two clusters of $\Delta^{12}CH_2D_2$ values obtained in this study could be translated into the estimated temperatures of 60±10°C and 200±50°C (Figure S4b). The lower one (60±10°C) is derived from the samples collected from the Chishan fault (SYNH-01 and WSD) and offshore sediments. All samples from the Chishan fault possess bulk isotopic compositions interpreted as thermogenic methane, and $\Delta^{13}CH_3D$ and $\Delta^{12}CH_2D_2$ values close to the equilibrium curve. For comparison, bulk isotopic compositions of methane for marine sediments indicate typical microbial origin. If the hypothetical re-equilibration proceeds with the variation in $\Delta^{13}CH_3D$ value only, the re-equilibration would occur at the temperature (60±10°C), which is lower than the gas window commonly considered for the formation of thermogenic

methane (>80°C) (Pepper & Corvi, 1995). The scenario is unlikely unless the catalyst involved in the re-equilibration is sufficiently efficient to facilitate the intra-molecular re-ordering of methane isotopologues at that low temperature. Instead, the data distribution (both bulk isotopic and clumped compositions) could be best explained by the mixing between a thermogenic end component and a microbial end component represented by the offshore sediments (Figure S5; see section 5.3 for details).

(2) The cluster with higher projected temperatures (200±50°C) (Figure S4b) encompasses several sub-clusters spanning over 30‰ of $\Delta^{12}CH_2D_2$ values. Values off the equilibrium line were derived from samples collected from the Chukou fault, Chishan fault, Gutingkeng anticline, and Coastal Plain. For samples from the Chukou and Chishan faults, the majority of their $\delta^{13}C$ and $\delta^{2}H$ values are interpreted as thermogenic in origin (with the exception of YSES). For comparison, all samples from the Gutingkeng anticline and Coastal Plain possessed $\delta^{13}C$ and $\delta^{2}H$ values categorized as a mixture of microbial and thermogenic origin. By examining the details, the projected temperatures of re-equilibration based on $\Delta^{12}CH_2D_2$ values range around 200°C and could reach as high as 686°C (Table S2). If the former projected temperature represents a temperature of re-equilibration, the re-equilibration would proceed with a burial of approximately 7 km depth (assuming the geothermal gradient is 25°C/km; Chi and Reed, 2008) following the initial formation through either microbial process or thermal maturation. Since the disequilibrium clumped isotopic composition for thermogenic methane has not been affirmatively validated for environmental samples (Shuai et al., 2018; Xia & Gao, 2019), only the scenario for the re-equilibration of microbial methane is addressed here. Although the temperature limit to life or methanogenesis could range up to 122°C (Takai et al., 2008), the formation of microbial methane in petroleum or natural gas systems is generally considered to take place at temperature less than 80°C (Head et al., 2003). In this regard, at least additional ~5 km of burial after its initial formation is presumably needed to reach the temperature for the designated re-equilibration. To assess this possibility, the uplift history of Taiwan orogenesis that has accommodated the shortening between the Luzon arc and the Eurasian plate is utilized. While the collision started at about 5 Ma (based on the first appearance of slate fragments in the sedimentary records; Teng, 1987), the uplift and exhumation accelerated during the period of 1-2 Ma (Chen et al., 2023; Lee et al., 2022). If the uplift rate of 1 cm/yr is

assumed (Chen et al., 2023; Yen et al., 2008), a total of 1000-2000 m of uplift would be expected. The estimate does not take erosion (up to 5 mm/yr based on ^{10}Be dating; Fellin et al., 2017) into account and should be considered an optimum scenario. This quantity could also be translated into the burial of the formations in the footwall of thrust faults. Unless the uplift rate could be raised by at least a factor of 2.5 and the erosion could be ignored, the estimated optimum burial is apparently not sufficient to reach the designated re-equilibration temperature.

(3) Some of the data points for the high temperature cluster were distributed at $\Delta^{12}CH_2D_2$ values of less than 4 (samples collected from the Chukou fault, Gutingkeng anticline, and Coastal Plain). If these data points are attributed to the hypothetical re-equilibration, then the re-equilibration temperatures could be at least 261^{o}C and reach as high as 686^{o}C (Table S2). Such a temperature range requires an unlikely burial depth as being described and exceeds the upper bound for thermal maturation. Again, the data distribution could not be accounted for by re-equilibration.

For microbial methane oxidation, bulk isotope compositions for residue methane would generally increase with the extent of consumption (Whiticar, 1999). Depending on the fractionation factors, the enrichment in heavier isotopes would vary considerably among species or environmental characteristics. In contrast, the clumped isotopic compositions exhibit drastically different patterns between aerobic and anaerobic methane oxidation based on culture, enrichment, and environmental observations. The $\Delta^{13}CH_3D$ and $\Delta^{12}CH_2D_2$ values either decrease off or along the equilibrium curve for aerobic methane oxidation (Giunta et al., 2022; Krause et al., 2022), or cluster close to or along the equilibrium curve and its extension off 0^{o}C mark or vary off the equilibrium curve and along the $\Delta^{12}CH_2D_2$ axis for AOM (Ash et al., 2019; Giunta et al., 2022; Liu et al., 2023; Ono et al., 2021). In one case for the Baltic Sea sediments (Ash et al., 2019), a methanogenic zone is sandwiched by two sulfate-methane transition zones (SMTZ) attributed to the sulfate- and Fe-AOM. The $\Delta^{13}CH_3D$ and $\Delta^{12}CH_2D_2$ values for the deep SMTZ are nearly constant, reaching a thermodynamic equilibrium at a temperature consistent with the in situ 7.8^{o}C. The results obtained from the Black Sea sediments, on the other hand, exhibit a different pattern (Giunta et al., 2022). Their $\Delta^{13}CH_3D$ and $\Delta^{12}CH_2D_2$ values are close to the equilibrium curve at the bottom of SMTZ and increase to a highly enriched level (15-16‰ for $\Delta^{13}CH_3D$ and 60-75‰ for $\Delta^{12}CH_2D_2$) at the top of the SMTZ, a pattern

554 also observed in the incubations of AOM enrichments from Svalbard sediments (Liu
555 et al., 2023). For comparison, the potential AOM in seep sediments (from Santa
556 Barbara Channel) and deep materials (Nankai sediments and Beatrix fluids) shift the
557 $\Delta^{13}CH_3D$ value toward the thermodynamic equilibrium with the insignificant change
558 in $\Delta^{12}CH_2D_2$ value (Liu et al., 2023). The contrast patterns of isotopologue
559 abundances have been linked to the reversibility of methane oxidation potentially
560 controlled by the thermodynamic drive intrinsically linked to the availability of
561 sulfate and methane (Liu et al., 2023). For abundant substrate (and energy flow) like
562 that attested by culture experiments (Ono et al., 2022), AOM is regulated by kinetic
563 effects that lead to the disequilibrium isotopologue abundances. In contrast, AOM
564 imposed by limited substrate availability proceeds with the high reversibility so
565 thermodynamic equilibrium could be readily reached (Liu et al., 2023). Various
566 thresholds of the substrate availability have been proposed primarily based on field
567 observations (Ash et al., 2019; Giunta et al., 2022; Ono et al., 2021), thereby
568 warranting the validation from laboratory tests.
569 To address the potential of AOM for this study, the distribution of $\Delta^{13}CH_3D$ and
570 $\Delta^{12}CH_2D_2$ values was first examined. Only two seep sediments (FWCR and FR)
571 possess $\Delta^{13}CH_3D$ and $\Delta^{12}CH_2D_2$ values resembling those from the Baltic and Black
572 Seas near the equilibrium curve at the low temperature end. However, these two
573 sediments were retrieved from the gas hydrate stability zone at a depth of 108 m for
574 FWCR and 22 m for FR below the seafloor. Based on the geochemical characteristics
575 (Bohrmann et al., 2023), these samples are not representative of sediments typical for
576 AOM. Furthermore, the data points for mud volcanoes in western Taiwan (Figure S4)
577 are not near the low temperature end of the equilibrium line but resemble the shift
578 caused by potential AOM that proceeds with high reversibility under or near
579 thermodynamic threshold (Liu et al., 2023). Although sulfate-AOM at <10 cm depth
580 has been validated based on the geochemical profile and genetic data for SYNH
581 (Cheng et al., 2012; Lin et al., 2018), these samples were collected from the mud
582 platform formed by the accumulation of fluidic mud emanating from the bubbling
583 pool. Here, sulfate-AOM is fueled by methane percolating off the major fluid conduit
584 and through the porous medium, and by sulfate generated by the oxidation of pyrite or
585 iron sulfide through the exposure of deeply sourced sediments to the atmosphere
586 (Cheng et al., 2012; Lin et al., 2018). As our samples were collected from the

bubbling pools that represent the surface expression of subsurface fluid channels, collected gases were plumbed from the deep source with minimum alteration during the transport, thereby exhibiting geochemical and community composition patterns distinct from those in the mud platform (Cheng et al., 2012; Lin et al., 2018). Similarly, aerobic methane oxidation has been validated with geochemical, incubation, and genetic data for the mud platform sediments at SYNH (Cheng et al., 2012; Lin et al., 2018). Again, companion data for samples collected from bubbling pools are distinct from those from the mud platform. The bulk and clumped isotopic compositions for our samples were also not aligned with the ranges commonly attributed to aerobic methane oxidation (Figures 2 and 3). Taken together, while these lines of evidence do not favor microbial methane oxidation (either anaerobic or aerobic style) as the main cause of isotopic variations, the possibility of AOM could not be completely ruled out.

Finally, molecular diffusion has been considered to address the isotopic variations (both bulk and clump isotopes) (Giunta et al., 2021). The tenuous nature of diffusive pathway in sedimentary rocks would particularly enable the mass-differentiation transport during fluid percolation over a long-distance range. According to the rules of mass difference (Etiope et al., 2009), diffusion facilities to transport lighter isotopes over heavier ones, resulting in the preferential depletion of ^{13}C or smaller $\delta^{13}C/\delta^{2}H$ values for migratory methane (or vice versa for residue methane). On the other hand, the corresponding $\Delta^{12}CH_2D_2$ vs. $\Delta^{13}CH_3D$ values would increase (Giunta et al., 2021). Both these variation trends follow a 1:1 slope in the $\delta^{2}H$ vs. $\delta^{13}C$ and $\Delta^{12}CH_2D_2$ vs. $\Delta^{13}CH_3D$ plots (Figure S4; constrained by the beta value (0.05) for single or double substituted isotopologues). Either plot for the data reported in this study reveals that diffusion seems to account for multiple linear distributions of isotopic compositions (Figure S4). However, if a $\delta^{13}C$ value of -33‰ (CLP; thermogenic methane) is used to anchor one end of the diffusion trend in the plot of $\Delta^{13}CH_3D$ vs. $\delta^{13}C$ (Figure S4), it is apparent that the variations in $\delta^{13}C$ value is not sufficient to account for those in $\Delta^{13}CH_3D$ value (nearly all data points plotted above the diffusion trend). If diffusion is the governing mechanism for isotopic fractionation, the anchor point in $\delta^{13}C$ axis has to be set at a higher value (> -20‰), a scenario more likely representing abiotic source and not supported by the current data. Again, diffusion could not explain the data variation.

Overall, the data pattern, geological context, and the projected temperature based on individual isotopologue abundance are not in favor of the re-equilibration, microbial methane oxidation, and diffusive transport as a broad-scaled control on the variations in bulk and clumped isotopic compositions. For those clumped isotopic compositions off the equilibrium line, the mixing between thermogenic and microbial sources appears to be the most plausible explanation for most samples (see section 5.3 for details). Since these samples are distributed in several structural domains, the exchange of fluids and gases between domains is unlikely. Lumping all data together across structural domains could have potentially masked the intrinsic characteristics associated with primary and secondary mechanisms responsible for the formation or alteration of methane for individual structural domains or samples. To unequivocally discern methane origins in such a tectonically complex and fragmented terrain like Taiwan, a wider coverage of sampling with designated targets and designed laboratory experiments is warranted.

5.3 Mixing of methane, helium, and nitrogen between sources

The isotopologue abundances provide an extra dimension to account for a mixed origin, in addition to bulk isotopic compositions and abundance ratios. The mixing scenarios are discussed here in accordance with the structural domains. As the exact mechanisms and characteristics of abiotic methane are still vague, the mixing scenarios are limited to using thermogenic and microbial end components. In principle, the highest estimated temperatures based on isotopologue abundances for the individual structural domain were selected as the thermogenic end component. Results obtained from culture experiments (Young et al., 2017; Giunta et al., 2019) were first used as the microbial end component. Other than that, environmental samples indisputably attributed to methanogenesis could also be considered. To avoid of arbitrary designation, it would be even better if the target samples and environmental samples treated as the end component could belong to a similar/same geological context. Therefore, the potential heterogeneity of the end component compositions would be taken into account. Regardless of which end component is chosen, the mixing scenarios based on bulk and clumped isotopic compositions should be coherent. For sites along the Chishan fault, methane from some sites (SYNH-01 and WSD-01) was partially produced by secondary CO_2 reduction (see

653 section 5.1). Their bulk isotopic compositions slightly deviated from the potential end
654 component of thermal maturation ascribed to SYNH-02. To quantify the contribution
655 of thermogenic versus microbial methane, mass conservation was first applied with a
656 thermogenic end component represented by $\delta^{13}C_{CH4}$ of -35.3‰ and $\delta^{2}H_{CH4}$ of
657 -143.6‰ (site SYNH-02), and a microbial end component represented by average
658 culture values for either CO_2 reduction methanogenesis ($\delta^{13}C_{CH4}$ of -51.1‰ and
659 $\delta^{2}H_{CH4}$ of -389.4‰) or methylotrophic methanogenesis ($\delta^{13}C_{CH4}$ of -45.8‰ and
660 $\delta^{2}H_{CH4}$ of -299.4‰) (Young et al., 2017; Giunta et al., 2019). For sites SYNH-01 and
661 WSD-01, their similar bulk isotopic compositions both yielded 10% and 25%
662 contributions of microbial methane from CO_2 and methylated compounds,
663 respectively (Figure S5). Similar approaches were adopted in the isotopologue mixing
664 model ($\Delta^{13}CH_3D$ of 2.13‰ and $\Delta^{12}CH_2D_2$ of 5.47‰ from site SYNH-02 for the
665 thermogenic end component; $\Delta^{13}CH_3D$ of 2.90‰ and $\Delta^{12}CH_2D_2$ of -16.46‰ from
666 methanogens in laboratory (Giunta et al., 2019; Young et al., 2017) as the average
667 microbial end component). The calculation yielded a 60% microbial fraction for site
668 SYNH-01, and 45% for site WSD-01, from CO_2 reduction methanogenesis (Figure
669 S5). For comparison, the isotopologue mixing model based on methylotrophic
670 methanogenesis could not replicate the observations.
671 Marine sediments collected offshore Taiwan (FR and FWCR) as the potential
672 microbial end component were also assessed. These two samples possessed bulk
673 isotopic compositions typical for microbial methane ($\delta^{13}C_{CH4}$ of -69‰ and $\delta^{2}H_{CH4}$ of
674 -190‰). Their clumped isotopic compositions were, however, distinct from the
675 culture representatives, and distributed off the equilibrium line (Figure 2) in the space
676 occupied with a number of data points from marine sediments (Ash et al., 2019;
677 Giunta et al., 2022). The mixing scenarios are not coherent between clumped and bulk
678 isotopic compositions. While the isotopologue mixing model yielded a microbial
679 contribution ranging from 20% to 60%; Figure S5), the bulk-based mixing model
680 yielded a much less microbial contribution (<10%) with greater uncertainties.
681 For sites in the Chukou fault, the Gutingkeng anticline, and the Coastal Range, a
682 mixing model was constructed using a similar thermogenic end component (KTL for
683 the Chukou fault, SYNH-02 for the Gutingkeng anticline, and LS for the Coastal
684 Range) and a microbial end component derived from marine sediments (either
685 FR/FWCR values or $\delta^{2}H_{CH4}$ and $\Delta^{12}CH_2D_2$ values slightly smaller than FR/FWCR

686 values). The calculations for bulk isotopic and isotopologue mixing yielded
687 comparable fractions (40% to 80% for bulk isotope mixing and 20% to 90% for
688 isotopologue mixing) of the microbial end component (Figure S5), a pattern
689 consistent with the detection of methanogens using different substrates in these
690 regions (Chang et al., 2012; Ling et al., 2012; Wang et al. 2014).

691 Helium isotopic ratios ranged from 0.1 to 6.8 Ra (Figure 3; Table S4). Most ratios
692 (except for sites AT, CLP, CLS, TDS, GI, and LS) were smaller than 1 Ra, indicating
693 that the gases originated from a crustal component. The N_2 isotopologue results
694 appear to be correlated with helium isotopes. Three sites (KTL-02, WSD-01, and AT)
695 showed Δ_{30} values ranging between +11‰ and +17‰ (Figure S3; Table S3;). This is
696 lower than the air value of +19.3‰ (Yeung et al., 2017) but much higher than 0‰
697 observed for crustal and volcanic nitrogen (Labidi et al., 2020), suggesting the
698 addition of the air to deep crustal/volcanic nitrogen. A mass balance calculation
699 yielded that 40-80% of the N_2 in the gas mixtures must be accounted for by the
700 air-derived nitrogen. In other words, the nitrogen with a deep origin with a Δ_{30} value
701 of 0‰ (Labidi et al., 2020) contributed to 20-60% of the gas mixtures. While no
702 robust $\delta^{15}N$ estimate could be provided for the crustal nitrogen end component, $\delta^{15}N$
703 values tend to vary towards a more negative range (-2.1‰) for the samples with the
704 highest air contributions. This likely reflects mass-dependent fractionation of
705 atmospheric nitrogen in the subsurface (Labidi and Young, 2022), rather than a
706 signature from deep nitrogen. The Δ_{30} pattern for KTL and WSD in the Western
707 Foothills is consistent with crustal helium signatures and methane formations at
708 temperatures of 260^{o}C (for KTL). However, the deep nitrogen source for AT in the
709 Coastal Range is not necessarily only the crustal component. Its $^{3}He/^{4}He$ ratio is
710 relatively high (2.3 Ra), suggesting a mixture between mantle and air/crust. The bulk
711 and clumped isotopic compositions of methane are interpreted as the abiotic origin
712 with the formation temperature or depth unconstrained (see sections 5.1 and 5.4 for
713 details). If nitrogen shares the same source of helium, the deep source is at least
714 partially composed of the mantle component. For comparison, the two GI duplicates
715 with 6.7 Ra and 6.8 Ra showed Δ_{30} values of 3.1‰ and 1.8‰, a range close to 0‰.
716 This likely reflects marginal (<10%) air contributions. Their $\delta^{15}N$ values were +3.6‰,
717 a pattern consistent with the signature associated with subducted nitrogen, which is
718 later accumulated in sub-arc mantle sources worldwide (Busigny et al., 2011, Epstein

et al., 2021, Labidi et al., 2021), and previously hypothesized to contribute nitrogen to surface vents in Taiwan (Roulleau et al., 2015). Together with mantle-derived helium, the recycled nitrogen must have been remobilized towards the surface via volcanism followed by hydrothermal interactions.

While the origins of methane from sites CLP, CLS, TDS, and LS could be constrained by bulk isotopic and isotopologue compositions, and abundance ratios (thermogenic for sites CLP, CLS and LS, and microbial for site TDS), their anomalous helium isotopic compositions deserve special attentions. The analyses yielded $^{3}He/^{4}He$ ratios that ranged from 1.8 Ra (TDS and LS) to 5.4 Ra (CLP and CLS) and were comparable with data reported previously for sites CLP, CLS (Fu et al., 2021), and LS (Yang et al., 2003). The values suggest a mixture between crustal (0.01 Ra) and mantle components (>8 Ra) (Poreda & Craig, 1989). Except for site LS, the involvement of a mantle contribution is intriguing since the other three sites are all part of the accretionary prism with sporadic volcanism that dates back to 17 Ma and is potentially associated with the opening of the South China Sea (Chen, 2016). These igneous rocks in the subsurface might serve to account for the continuous degassing of helium with mantle signatures. Alternatively, the supply of helium with mantle signatures could have been along the fault or fracture network extending to the mantle depth. In this regard, helium with mantle signatures should have pervasively infiltrated into the fracture systems of the accretionary prism and been observed at a regional scale, which is not the case in this study. For site LS, the impingement of the Luzon Arc on the Eurasian continent has emplaced numerous igneous bodies in the Coastal Range. Like what has been observed for site GI, helium with mantle signatures could have originated from the igneous intrusion in the subsurface. Regardless of the source region, methane and hydrocarbons from igneous bodies are generally considered to possess abiotic signatures, which were not observed for sites associated with sedimentary formations (CLP, CLS, TDS, and LS) but were consistent with the arc setting for sites AT and GI.

Overall, the origins of methane, helium, and nitrogen gases could have been segregated into different compartments of the subduction system. Therefore, their individual mixing patterns would not be necessarily coupled but rather reflect the complexity of sources, transport paths, and fracture connectivity in the tectonically fragmented terrain of Taiwan.

752

753 5.4 Potential abiogenic methane in the Coastal Range

754 The methane recovered from sites AT and GI is interpreted as originating from
755 abiotic Fischer-Tropsch Type processes. Their $\Delta^{13}CH_3D$ and $\Delta^{12}CH_2D_2$ values
756 (Figure 2) overlap with the range for abiotic methane reported in previous studies
757 (Young et al., 2017) and are distributed near (for site GI) or on the equilibrium line
758 (for site AT; corresponding to ~23°C) (Figure 2). Laboratory constraints have shown
759 that such surface catalyzed reactions between hydrogen and CO or CO_2 on different
760 metal sulfides proceed at temperatures between 70°C and 600°C (Etiope & Lollar,
761 2013). Field observations and interpretations that combined bulk isotopic
762 compositions, abundance ratios, and water/geological characteristics for regions with
763 prevalent serpentinization have further extended the possible temperature to between
764 50°C and 500°C (Etiope & Lollar, 2013). Limited experiments, however, have shown
765 that methane synthesized from the Sabatier reactions catalyzed by Ru at 70-600°C
766 yielded $\Delta^{13}CH_3D$ and $\Delta^{12}CH_2D_2$ values either on the high temperature end of the
767 equilibrium line (>400°C) or distributed over a wide range below the equilibrium line
768 ($\Delta^{13}CH_3D$ between 0‰ and +4.5‰ and $\Delta^{12}CH_2D_2$ between -55‰ and 0‰) (Young et
769 al., 2017). For comparison, $\Delta^{13}CH_3D$ and $\Delta^{12}CH_2D_2$ values for Chimaera and Kidd
770 Creek samples attributed to abiotic in origin are distributed either along the segment
771 of the equilibrium line between 25°C and 150°C or below the equilibrium line (Young
772 et al., 2017). The data pattern obtained in this study is distinct from the experimental
773 constraints but resembles the field observations. However, the temperature estimate
774 based on isotopologue abundances is much lower than the field observation for site
775 AT (23°C versus 62°C). Such temperature contradiction suggests that both
776 isotopologues do not reach internal equilibrium and thus do not record a true
777 formation temperature. In addition, helium isotopic compositions for sites GI and AT
778 were 6.7 Ra and 2.4 Ra, respectively (Table S4). This range of helium isotope
779 compositions suggests a higher mantle fraction and is comparable with the proximity
780 to igneous bodies associated with the arc impingement. Overall, the close
781 resemblance of isotopologue abundances between these two sites and Chimaera/Kidd
782 Creek combined with the higher contribution of mantle helium reinforces the
783 interpretation that methane from these two sites is abiotic in origin. The formation
784 could have proceeded at temperatures slightly lower than those imposed by

785 experimental constraints. Alternatively, post-formation resetting of abiotic methane
786 isotopologues, dominated by changes in $\Delta^{12}CH_2D_2$ as described by Labidi et al. (2020)
787 might explain the shift from a purely abiotic isotopologue signature to one near
788 equilibrium at lower temperatures, although the temperature disparity remains. The
789 possibility that the abiogenic-like signatures are derived from AOM (Warr et al., 2021;
790 Giunta et al., 2022; see section 5.2 for more discussion), thermal maturation of
791 organic matters circulated from surface waters (Fiebig et al., 2019) or biodegradation
792 of organic matters with H_2 produced by serpentinization (Xia & Gao, 2021) is noted.
793
794 5.5 Water isotopic compositions
795 Isotopic compositions of water fell within the range reported previously (Chao
796 et al., 2011; You et al., 2004). Among data points, several for sites LS and AT in the
797 Coastal Range, and site WF in the Chukou fault were distributed near or along the
798 global and local meteoric water lines (Peng et al., 2010; Figure 4a). While data
799 points for site GI clustered around a seawater composition (Table S5), all the other
800 data points deviated from the meteoric water line and exhibited various degrees of
801 ^{18}O enrichment (Figure 4a). By combining with previous results, two variation
802 trends could be drawn. The first one is composed of data points for the Chishan fault,
803 Gutingkeng anticline, and Coastal Plain, whereas the second one comprises data
804 points solely from the Chukou fault. Both trends share a common end component
805 enriched with ^{18}O ($\delta^{18}O_{H20}$ values were +7‰). The presence of such an ^{18}O-enriched
806 water is also observed in a previous study for the porewater retrieved from the TY
807 mud volcano offshore southwestern Taiwan, and could best be accounted for by deep
808 water derived from the smectite dehydration at 100-150°C (Chen et al., 2020). Using
809 the average geothermal gradient for the offshore region (25°C/km; Chi and Reed,
810 2008), the depth corresponding to the water formation has been estimated to range
811 between 3.6 km and 5.7 km below the seafloor (Chen et al., 2020). If this end
812 component is prevalent in the accretionary wedge across marine and terrestrial realms,
813 the water mixture would be bracketed by three end components, including deep
814 water (stated above), seawater-like water, and meteoric water.
815 For sites in the Chishan fault, Gutingkeng anticline, and Coastal Plain, the data
816 distribution (Figure 4a) suggests a greater contribution of seawater-like water over
817 meteoric water. Except for site TDS, most mud volcanoes in western Taiwan are

located at least 10 km from the shoreline (Figure S1). Therefore, the scenario of the seawater intrusion is less likely. Instead, the seawater-like composition could have been derived from relic seawater trapped during sedimentation. In contrast, for sites in the Chukou fault, the data distribution is aligned clearly with an end component comparable with the compositions of meteoric water retrieved from the southern plain or mountains (Peng et al., 2010).

Finally, the involvement of an end component resembling meteoric water suggests a short residence time of water circulation. Constraining the exact age or residence time of water from mud volcanoes is challenging as the tracers available for such a geological context are limited, and no data has been published to date. Site LS was chosen as an example to constrain the potential limit for the circulation of meteoric water as its water isotopic compositions fell on the local meteoric water line. Based on the isotopologue abundances, the temperature and depth for methane formation for site LS were estimated to be up to 90-100^{o}C and 2-3 km below the land surface, respectively. If this depth limit to the circulation of meteoric water is also applied to all mud volcanoes in the Western Foothills, a fast-track path from recharge of meteoric water to discharge along the fracture network at depths of less than 3 km would be required. To accommodate this possibility, the fracture opening derived from the depressurization and thrust displacement related to the rapid uplift and erosion is speculated to enable bedrock more permeable for recharge and deep penetration of water. The inference might not be the unique cause for tectonically fragmented terrains with rapid uplift and erosion (Chen et al., 2015; Dadson et al., 2003), as previous studies have demonstrated that isotopic compositions of cored calcite veins from a 2000-m deep borehole (Wang et al., 2010) and hot springs sampled from northern Taiwan are indicative of meteoric in origin (Chao et al., 2021; Lu et al., 2020). These results suggest that meteoric water could be recharged and circulated to deeper regions, heated up by the exhumed bedrocks that still preserve the relic heat associated with rapid uplift, and discharged along the fracture network to the surface outcrops.

The isotopic compositions of water suggest water circulation along different paths and the contribution of water compartmentalized in different source regions. For most samples from eastern Taiwan and few from western Taiwan, the meteoric nature further implied that water circulation is rapid with a short residence time in

the subsurface. Therefore, isotopic exchange between water and minerals is not substantially enough to alter the resultant water composition. In contrast, the majority of samples from western Taiwan bear the contribution of deep water that has experienced prolonged water-rock/mineral interactions. Water circulation along the divergent, and complex fracture network in the accretionary wedge enables the mixing process of deep water with either the formation water or meteoric water at shallow depths.

In addition to water origins, water isotopic compositions were used to constrain source characteristics of both water and methane. Estimated temperatures based on deuterium exchange between water and methane were compared with temperatures assessed by methane isotopologue abundances. The thermometer is adopted from Horibe and Craig (1995) using the following equation (for temperatures between 0°C and 370°C):

$$\alpha(H_2O_{Liq}/CH_4) = 1.0997 + 8456/T^2 + 0.9611 \times 10^9/T^4 - 27.82 \times 10^{12}/T^6 \quad \text{eq. 8}$$

where α is the ratio of $^2H/^1H$ of water to methane, and T is in Kevin.

For sites CLP, CLS, SYNH-02, and WD where isotopologue equilibrium is reached and deep water predominates over the other component, the temperatures estimated from the deuterium fractionations between methane and water ($\varepsilon_{CH4\text{-}H2O}$) correspond closely to the temperatures predicted by $\Delta^{13}CH_3D$ and $\Delta^{12}CH_2D_2$ values (Figure 4; Table S5). Comparable temperature estimates could be obtained for two additional sites (sites SYNH-01, and LCW) if only $\Delta^{13}CH_3D$ values were considered. For the equilibrium fractionation associated with deuterium exchange, two phases (methane and water) were involved. Therefore, comparable temperature estimates deduced from isotopic substitution within a phase and between phases suggest that methane and water shared a common source region, and the isotopic exchange between $^{13}CH_3D$ and water is more rapid than between $^{12}CH_2D_2$ and water. The $\Delta^{13}CH_3D/\Delta^{12}CH_2D_2$ values paired with $\varepsilon_{CH4\text{-}H2O}$ values for all the other sites fell off the equilibrium line (Figure 4). Since methane and water from these sites represent a mixture of different sources, isotopic exchange within a phase or between phases after mixing does not reach equilibrium, possibly due to insufficient time or a kinetic barrier imposed by the relatively low temperature. Finally, temperature estimates

based on paired isotopologue abundances were coherent for site LS in eastern Taiwan. However, the methane isotopologue abundances did not reach equilibrium with deuterium in the water. The data pattern contrasts with other studies (Giunta et al., 2019; Wang et al., 2015) and suggests that meteoric water percolating into the deep subsurface does not coexist with methane sufficiently long or methane is not completely dissolved in water to achieve isotopic equilibrium between phases. Again, consistent with the interpretation based solely on water isotopic compositions, the water circulation is likely rapid so the residence time is short.

5.6 Depth constraints using isotopologue-based temperature estimates

Our results indicated that the temperature estimates for sites CLP, CLS, KTL, SYNH-02, WD, and LS ranged from 99°C to 260°C (Table S2 and S6). Using measured local geothermal gradients (Chi & Reed, 2008) and assuming a surface temperature of 20°C, the methane generation depth was estimated to range from 2 to 9 km. The sites where methane reaches internal equilibrium are primarily distributed in three major structural features: sites CLP, CLS, and KTL in the Chukou fault, site SYNH-02 in the Chishan fault, and site LS in the Longitudinal Valley fault. The Chukou fault is an east dipping thrust oriented NE-SW (Yeh et al., 2016). Balanced cross sections suggest that the fault probably represents a complex fault system with subsurface branches forming an imbricate structure and an anticline underneath (Yeh et al., 2016). The fault and its branches are generally parallel to bedding within the Miocene formation and could be considered as part of the detachment fault extending to a depth of 7-8 km. The depth estimate ranged from 7-8 km for site CLP, to 4-5 km for site CLS, and to 6-8 km for site KTL (Figure 5a). As the formations are deformed and fragmented, water and gas transport could follow multiple routes interconnected to each other. Therefore, the estimated depth could be representative of the detachment fault and its related fracture system. For comparison, the Chishan fault is a high-angled, east dipping thrust with a left lateral component, and represents one of the branches of the detachment fault propagating westward (Rau et al., 2012). The depth estimates for site SYNH-02 were 8–9 km (Figure 5b), a range deeper than that reported for sampling in 2017 (Rumble et al., 2018; Supporting information) and coinciding with the extension of the detachment fault (10-12 km) in the region (Chen, 2016). The occurrence is also consistent with the origin of

^{18}O-enriched water retrieved from sites SYNH-01 and -02. Site WD is located further west of site SYNH-02 in the Coastal Plain and is not associated with any apparent fault outcrop. Based on seismic reflection, mud diapirism oriented NE-SW offshore this region has been identified (Chen et al., 2014). Site WD is aligned well with the onshore extension of one of the offshore mud diapirs. Whether the estimated formation depth of 7 km corresponds to the base of mud diapir or the detachment fault remains uncertain. Regardless of the source characteristics, its water isotopic composition is comparable with that of site SYNH-02 and the designated deep water. Finally, the Longitudinal Valley fault is the plate boundary thrust with a high angle dipping east and a left lateral sense (Chang et al., 2000). The hanging wall formation (Lichi formation) hosts site LS, and is composed of unlithified clays with rock fragments of various lithologies (e.g., ultramafic, meta-sandstone) (Chen et al., 2007). This combined with intensively shearing suggests its intimate relationship with the subduction. The depth estimate of 2-3 km (Figure 5c) for this site probably corresponds to a source region at the base of the Lichi formation intersected by the Longitudinal Valley fault.

6. Conclusions

Our methane isotopologue results combined with helium, nitrogen, water, and CO_2 related isotopic compositions reveal a spectrum of geochemical characteristics that point to diverse formation mechanisms and conditions for gases and water emanating from mud volcanoes, seeps, and springs investigated. Thermogenic methane was formed at temperatures ranging between 99°C and 260°C and appears to constitute a major component of hydrocarbons. The depths (2-9 km) corresponding to the estimated temperatures suggest a strong structural control that influences water and gas pathways. Thermogenic methane from a deep source is likely mixed by various degrees with abiotic methane pertinent to igneous bodies emplaced during subduction/collision, or microbial methane at shallow depths prior to being discharged to the atmosphere or seawater. Our results also suggest the potential decoupling of methane from water or helium sources, and an evolving depth range or mixing contribution for methane formation. Such patterns are consistent with active orogenesis, where gas and water channeling can undergo temporal and spatial variations associated with terrain fragmentation and dynamic structural control over

the course of mountain building.

Acknowledgments

We are grateful to the aid for sample and core retrievals by Nai-Chen Chen, Jui-Fen Tsai, Ling-Ho Chung, Tourism Bureau of Tainan City Government, Agriculture Bureau of Kaohsiung City Government, Zhaori Hot Spring of Taitung County Government, and the captain and crew members of R/V Sonne (cruise SO266/1). The MARUM-MeBo200 team and David Wunsch (CORSYDE International GmbH & Co. KG; Berlin) are sincerely thanked for the preparation and deployment of the MeBo pressure core samplers during cruise SO266/1. We extend our gratitude to Dr. George Burr at National Taiwan University for English editing this manuscript.

Grant supports from Taiwanese Ministry of Education and Ministry of Science and Technology (MOST107-3113-M-002-004) are acknowledged. Cruise SO266/1 was funded by the German Ministry of Education and Science, project TaiDrill – SO266.

Open Research

All new data reported in the study are available on tables in the main manuscript and supporting information, and are archived at Lin et al. (2023).

References

Ash, J.L., Egger, M., Treude, T., et al. (2019). Exchange catalysis during anaerobic methanotrophy revealed by $^{12}CH_2D_2$ and $^{13}CH_3D$ in methane. *Geochemical Perspectives Letters*, 26-30. doi:10.7185/geochemlet.1910

Beaudry, P., Stefánsson, A., Fiebig, J., et al. (2021). High temperature generation and equilibration of methane in terrestrial geothermal systems: Evidence from clumped isotopologues. *Geochimica et Cosmochimica Acta*, 309, 209-234. doi:10.1016/j.gca.2021.06.034

Bernard, B.B., Brooks, J.M., & Sackett, W.M. (1977). A geochemical model for characterization of hydrocarbon gas sources in marine sediments. *Paper presented at the Offshore Technology Conference*. doi:10.4043/2934-MS

Bohrmann, G., Berndt, C., Lin, S., et al. (2023). Geological controls on the

983 distribution of gas hydrates in the shallow parts of the gas hydrate stability zone–
984 constraints from seafloor drilling off Taiwan. *Marine and Petroleum Geology*,
985 106253. doi:10.1016/j.marpetgeo.2023.106253
986 Bonilla, M.G. (1975). A Review of Recently Active Faults in Taiwan: U.S. Geological
987 Survey Open-File Report 75-41 Version 1.1.
988 Busigny, V., Cartigny, P., & Philippot, P. (2011). Nitrogen isotopes in ophiolitic
989 metagabbros: A re-evaluation of modern nitrogen fluxes in subduction zones and
990 implication for the early Earth atmosphere. *Geochimica et Cosmochimica Acta*, 75,
991 7502-7521. doi:10.1016/j.gca.2011.09.049
992 Campeau, A., Wallin, M. B., Giesler, R., et al. (2017). Multiple sources and sinks of
993 dissolved inorganic carbon across Swedish streams, refocusing the lens of stable C
994 isotopes. *Scientific reports,* 7, 9158. doi:10.1038/s41598-017-09049-9
995 Carson, B., & Screaton, E.J. (1998). Fluid flow in accretionary prisms: Evidence for
996 focused, time-variable discharge. *Reviews of Geophysics*, 36, 329-351.
997 doi:10.1029/97rg03633
998 Central Geological Survey; https://twgeoref.moeacgs.gov.tw
999 Central Weather Bureau;
1000 https://scweb.cwb.gov.tw/en-US/earthquake/details/2017021101125257008
1001 Chang, C.P., Angelier, J., & Huang, C.Y. (2000). Origin and evolution of a mélange:
1002 the active plate boundary and suture zone of the Longitudinal Valley, Taiwan.
1003 *Tectonophysics,* 325, 43-62. doi:10.1016/S0040-1951(00)00130-X
1004 Chang, Y.H., Cheng, T.W., Lai, W.J., et al. (2012). Microbial methane cycling in a
1005 terrestrial mud volcano in eastern Taiwan. *Environmental Microbiology*, 14,
1006 895-908. doi:10.1111/j.1462-2920.2011.02658.x
1007 Chao, H.C., Pi, J.L., You, C.F., et al. (2021). Hydrogeology constrained by
1008 multi-isotopes and volatiles geochemistry of hot springs in Tatun Volcanic Group,
1009 Taiwan. *Journal of Hydrology*, 600, 126515. doi: 10.1016/j.jhydrol.2021.126515
1010 Chao, H.C., You, C.F., & Sun, C.H. (2010). Gases in Taiwan mud volcanoes:
1011 Chemical composition, methane carbon isotopes, and gas fluxes. *Applied*
1012 *Geochemistry*, 25, 428-436. doi:10.1016/j.apgeochem.2009.12.009
1013 Chao, H.C., You, C.F., Wang, B.S., et al. (2011). Boron isotopic composition of mud
1014 volcano fluids: ImplCHANGications for fluid migration in shallow subduction
1015 zones. *Earth and Planetary Science Letters,* 305, 32-44.

doi:10.1016/j.epsl.2011.02.033

Chasar, L., Chanton, J., Glaser, P.H., et al. (2000). Radiocarbon and stable carbon isotopic evidence for transport and transformation of dissolved organic carbon, dissolved inorganic carbon, and CH_4 in a northern Minnesota peatland. *Global Biogeochemical Cycles,* 14, 1095-1108. doi:10.1029/1999GB001221

Chen, A.T., Sano, Y., Byrne, T.B., et al. (2020). Helium Isotopic Signature of a Plate Boundary Suture in an Active Arc–Continent Collision. *Earth and Space Chemistry*, 4, 1237-1246. doi:10.1021/acsearthspacechem.0c00038

Chen, N.C., Yang, T.F., Hong, W.L., et al. (2020). Discharge of deeply rooted fluids from submarine mud volcanism in the Taiwan accretionary prism. *Scientific reports,* 10, 381. doi:10.1038/s41598-019-57250-9

Chen, N.C., Yang, T.F., Hong, W.L., et al. (2017). Production, consumption, and migration of methane in accretionary prism of southwestern Taiwan. *Geochemistry, Geophysics, Geosystems,* 18, 2970-2989. doi:10.1002/2017GC006798

Chen, S.C., Hsu, S.K., Tsai, C.H., et al. (2010). Gas seepage, pockmarks and mud volcanoes in the near shore of SW Taiwan. *Marine Geophysical Researches*, 31, 133-147. doi:10.1007/s11001-010-9097-6

Chen, S.C., Hsu, S.K., Wang, Y., et al. (2014). Distribution and characters of the mud diapirs and mud volcanoes off southwest Taiwan. *Journal of Asian Earth Sciences*, 92, 201-214. doi:10.1016/j.jseaes.2013.10.009

Chen, W.S., Yen, I.C., Fengler, K.P., et al. (2007). Late Holocene paleoearthquake activity in the middle part of the Longitudinal Valley fault, eastern Taiwan. *Earth and Planetary Science Letters,* 264, 420-437. doi:10.1016/j.epsl.2007.09.043

Chen, W.S. (2016). *An introduction to the geology of Taiwan* (in Chinese). Geological Society Located in Taipei.

Cheng, T.W., Chang, Y.H., Tang, S.L., et al. (2012). Metabolic stratification driven by surface and subsurface interactions in a terrestrial mud volcano. *ISME J*, 6, 2280-2290. doi:10.1038/ismej.2012.61

Chen, Y. W., Shyu, J. B. H., & Chang, C. P. (2015). Neotectonic characteristics along the eastern flank of the Central Range in the active Taiwan orogen inferred from fluvial channel morphology. *Tectonics*, 34, 2249-2270. doi:10.1002/2014TC00379

Chi, W.C., & Reed, D.L. (2008). Evolution of shallow, crustal thermal structure from subduction to collision: An example from Taiwan. *Geological Society of America*

Bulletin, 120, 679-690. doi:10.1130/b26210.1

Chung, S.L., Yang, T.F., Lee, C.Y., et al. (1995). The igneous provinciality in Taiwan: consequence of continental rifting superimposed by Luzon and Ryukyu subduction systems. *Journal of Southeast Asian Earth Sciences*, 11, 73-80. doi:10.1016/0743-9547(94)00040-L

Chyi, L.L., Chou, C.Y, Yang, F.T., et al. (2001). Continuous radon measurements in faults and earthquake precursor pattern recognition. *Western Pacific Earth Sciences*, 1, 227-246. Doi: Code not available

Craig, H. (1961). Isotopic variations in meteoric waters. *Science,* 133, 1702-1703. doi:10.1126/science.133.3465.1702

Dadson, S. J., Hovius, N., Chen, H., et al. (2003). Links between erosion, runoff variability and seismicity in the Taiwan orogen. *Nature*, 426, 648-651. doi:10.1038/nature02150

Douglas, P.M., Stolper, D.A., Eiler, J.M., et al. (2017). Methane clumped isotopes: Progress and potential for a new isotopic tracer. *Organic Geochemistry*, 113, 262-282. doi:10.1016/j.orggeochem.2017.07.016

Epstein, G.S., Bebout, G.E., Christenson, B.W., et al. (2021). Cycling of CO_2 and N_2 along the Hikurangi subduction margin, New Zealand: An integrated geological, theoretical, and isotopic approach. *Geochemistry, Geophysics, Geosystems*, 22, e2021GC009650. doi:10.1029/2021GC009650

Etiope, G. (2009). Natural emissions of methane from geological seepage in Europe. *Atmospheric Environment,* 43, 1430-1443. doi:10.1016/j.atmosenv.2008.03.014

Etiope, G., & Lollar, B. (2013). Abiotic methane on Earth. *Reviews of Geophysics,* 51. doi:10.1002/rog.20011

Fellin, M.G., Chen, C.Y., Willett, S.D., et al. (2017). Erosion rates across space and timescales from a multi-proxy study of rivers of eastern Taiwan. *Global and Planetary Change*, 157, 174-193. doi:10.1016/j.gloplacha.2017.07.012

Fu, C.C., Lai, C.W., Yang, T.F., et al. (2021). An automatic system for continuous monitoring and sampling of groundwater geochemistry in earthquake-prone regions of SW Taiwan. *Frontiers in Earth Science,* 9. doi:10.3389/feart.2021.635913

Fiebig, J., Stefansson, A., Ricci, A., et al. (2019). Abiogenesis not required to explain the origin of volcanic-hydrothermal hydrocarbons. *Geochemical Perspectives*

Letters. 23-27. doi:10.7185/geochemlet.1920

Giunta, T., Young, E.D., Warr, O., et al. (2019). Methane sources and sinks in continental sedimentary systems: New insights from paired clumped isotopologues $^{13}CH_3D$ and $^{12}CH_2D_2$. *Geochimica et Cosmochimica Acta,* 245, 327-351. doi:10.1016/j.gca.2018.10.030

Giunta, T., Labidi, J., Kohl, I. E., et al. (2021). Evidence for methane isotopic bond re-ordering in gas reservoirs sourcing cold seeps from the Sea of Marmara. *Earth and Planetary Science Letters*, 553, 116619. doi:10.1016/j.epsl.2020.116619

Giunta, T., Young, E.D., Labidi, J., et al. (2022). Extreme methane clumped isotopologue bio-signatures of aerobic and anaerobic methanotrophy: insights from the Lake Pavin and the Black Sea sediments. *Geochimica et Cosmochimica Acta*, 338, 34-53. doi:10.1016/j.gca.2022.09.034

Head, I.M., Jones, D.M., & Larter, S.R. (2003). Biological activity in the deep subsurface and the origin of heavy oil. *Nature*, 426, 344-352. doi:10.1038/nature02134

Horibe, Y., & Craig, H. (1995). DH fractionation in the system methane-hydrogen-water. *Geochimica et Cosmochimica Acta,* 59, 5209-5217. doi:10.1016/0016-7037(95)00391-6

Horita, J., & Wesolowski, D.J. (1994). Liquid-vapor fractionation of oxygen and hydrogen isotopes of water from the freezing to the critical temperature. *Geochimica et Cosmochimica Acta*, 58, 3425-3437. doi: 10.1016/0016-7037(94)90096-5

Huang, S.T., Yang, K.M., Hung, J.H., et al. (2004). Deformation Front Development at the Northeast Margin of the Tainan Basin, Tainan–Kaohsiung Area, Taiwan. *Marine Geophysical Researches*, 25, 139-156. doi:10.1007/s11001-005-0739-z

Jautzy, J.J., Douglas, P.M., Xie, H., et al. (2021). CH_4 isotopic ordering records ultra-slow hydrocarbon biodegradation in the deep subsurface. *Earth and Planetary Science Letters*, 562, 116841.

Karakashev, D., Batstone, D.J., Trably, E., et al. (2006). Acetate oxidation is the dominant methanogenic pathway from acetate in the absence of Methanosaetaceae. *Applied and Environmental Microbiology*, 72, 5138-5141. doi:10.1128/AEM.00489-06

Klaucke, I., Berndt, C., Crutchley, G., et al. (2016). Fluid venting and seepage at

accretionary ridges: the Four Way Closure Ridge offshore SW Taiwan. *Geo-Marine Letters*, 36, 165-174. doi:10.1007/s00367-015-0431-5

Kietäväinen, R., & Purkamo, L. (2015). The origin, source, and cycling of methane in deep crystalline rock biosphere. Frontiers in Microbiology, 6, 725. doi:10.3389/fmicb.2015.00725

Kopf, A.J. (2003). Global methane emission through mud volcanoes and its past and present impact on the Earth's climate. *International Journal of Earth Sciences,* 92, 806-816. doi:10.1007/s00531-003-0341-z

Krause, S.J., Liu, J., Young, E.D., & Treude, T. (2022). $\Delta^{13}CH_3D$ and $\Delta^{12}CH_2D_2$ signatures of methane aerobically oxidized by *Methylosinus trichosporium* with implications for deciphering the provenance of methane gases. *Earth and Planetary Science Letters*, 593, 117681. doi:10.1016/j.epsl.2022.117681

Kunath, P., Chi, W.C., Berndt, C., et al. (2020). A shallow seabed dynamic gas hydrate system off SW Taiwan: Results from 3-D seismic, thermal, and fluid migration analyses. *Journal of Geophysical Research: Solid Earth*, 125, e2019JB019245-T. doi:10.1029/2019JB019245

Kunath, P., Crutchley, G., Chi, W.C., et al. (2022). Episodic venting of a submarine gas seep on geological time scales: Formosa Ridge, northern South China Sea. *Journal of Geophysical Research: Solid Earth*, 127, e2022JB024668. doi:10.1029/2022JB024668

Labidi, J., & Young, E. (2022). The origin and dynamics of nitrogen in the Earth's mantle constrained by $^{15}N^{15}N$ in hydrothermal gases. *Chemical Geology*, 591, 120709. doi:10.1016/j.chemgeo.2022.120709

Labidi, J., Young, E.D., Giunta, T., et al. (2020). Methane thermometry in deep-sea hydrothermal systems: Evidence for re-ordering of doubly-substituted isotopologues during fluid cooling. *Geochimica et Cosmochimica Acta*, 288, 248-261. doi:10.1016/j.gca.2020.08.013

Labidi, J., Young, E.D., Fischer, T.P., et al. (2021). Recycling of nitrogen and light noble gases in the Central American subduction zone: Constraints from $^{15}N^{15}N$. *Earth and Planetary Science Letters*, 571, 117112. doi:10.1016/j.epsl.2021.117112

Lacombe, O., Mouthereau, F., Deffontaines, B., et al. (1999). Geometry and Quaternary kinematics of fold-and-thrust units of southwestern Taiwan. *Tectonics*,

18, 1198-1223. doi:10.1029/1999TC900036

Lallemand, S. (2016). Philippine Sea Plate inception, evolution, and consumption with special emphasis on the early stages of Izu-Bonin-Mariana subduction. *Progress in Earth and Planetary Science*, 3, 15. doi:10.1186/s40645-016-0085-6

Lai, L.S.H., Roering, J.J., Finnegan, N.J., et al. (2021). Coarse sediment supply sets the slope of bedrock channels in rapidly uplifting terrain: Field and topographic evidence from eastern Taiwan. *Earth Surface Processes and Landforms*, 46, 2671-2589. doi:10.1002/esp.5200

Lee, Y.H., Byrne, T.B., Lo, W., et al. (2022). Out of sequence faulting in the backbone range, Taiwan: Implications for thickening and exhumation processes. *Earth and Planetary Science Letters*, 594, 117711. doi:10.1016/j.epsl.2022.117711

Lin, A.T., Liu, C.S., Lin, C.C., et al. (2008). Tectonic features associated with the overriding of an accretionary wedge on top of a rifted continental margin: An example from Taiwan. *Marine Geology,* 255, 186-203. doi:10.1016/j.margeo.2008.10.002

Lin, Y.T., Tu, T.H., Wei, C.L., et al. (2018). Steep redox gradient and biogeochemical cycling driven by deeply sourced fluids and gases in a terrestrial mud volcano. *FEMS Microbiology Ecology*, 94, 3796. doi:10.1093/femsec/fiy171

Lin, Y.T., Rumble, D., Young, E., Labidi, J., Tu, T.H., Chen, J.N. Pape, T., Bohrmann, G., Lin, S., Lin, L.H., and Wang, P.L. (2023). Supplementary Information for "Diverse origins of gases from mud volcanoes and seeps in tectonically fragmented terrane" [Dataset]. Zenodo. doi: 10.5281/zenodo.8275042.

Ling, Y.C., Chen, Y.J., Sun, C.H., et al. (2012). Potential of microbial methane formation in a high-temperature hydrocarbon seep. *Applied Geochemistry*, 27, 1666-1678. doi:10.1016/j.apgeochem.2012.04.002

Liu, J., Harris, R.L., Ash, J.L., et al. (2023). Reversibility controls on extreme methane clumped isotope signatures from anaerobic oxidation of methane. *Geochimica et Cosmochimica Acta*, 348, 165-186. doi:10.1016/j.gca.2023.02.022

Liu, C.S., Huang, I.L., & Teng, L.S. (1997). Structural features off southwestern Taiwan. *Marine Geology,* 137, 305-319. doi:10.1016/S0025-3227(96)00093-X

Lundegard, P.D., Sweeney, R.E., & Ririe, G.T. (2000). Soil gas methane at petroleum contaminated sites: Forensic determination of origin and source. *Environmental*

forensics, 1, 3-10. doi:10.1006/enfo.1998.0002

Lu, Y.C., Song, S. R., Lin, P. H., et al. (2020). Thermal Fluid Changes after Operating a Geothermal System: A Case Study of the Chingshui Geothermal Field, Taiwan. *Geothermics*, 87, 101878. doi: 10.1016/j.geothermics.2020.101878

Mazzini, A., & Etiope, G. (2017). Mud volcanism: An updated review. *Earth-Science Reviews*, 168, 81-112. doi:10.1016/j.earscirev.2017.03.001

Milkov, A.V. (2011). Worldwide distribution and significance of secondary microbial methane formed during petroleum biodegradation in conventional reservoirs. *Organic Geochemistry,* 42, 184-207. doi:10.1016/j.orggeochem.2010.12.003

Milkov, A.V., & Etiope, G. (2018). Revised genetic diagrams for natural gases based on a global dataset of >20,000 samples. *Organic Geochemistry,* 125, 109-120. doi:10.1016/j.orggeochem.2018.09.002

Mishima, K., Sumino, H., Yamada, T., et al. (2018). Accurate determination of the absolute $^{3}He/^{4}He$ ratio of a synthesized helium standard gas (Helium Standard of Japan, HESJ): toward revision of the atmospheric $^{3}He/^{4}He$ ratio. *Geochemistry, Geophysics, Geosystems,* 19, 3995-4005. doi:10.1029/2018GC007554

Ono, S., Rhim, J.H., Gruen, D.S., Taubner, H., et al. (2021). Clumped isotopologue fractionation by microbial cultures performing the anaerobic oxidation of methane. *Geochimica et Cosmochimica Acta*, 293, 70-85. doi:10.1016/j.gca.2020.10.015

Ono, S., Rhim, J.H., & Ryberg, E.C. (2022). Rate limits and isotopologue fractionations for microbial methanogenesis examined with combined pathway protein cost and isotopologue flow network models. *Geochimica et Cosmochimica Acta*. doi:10.1016/j.gca.2022.03.017

Ono, S., Wang, D.T., Gruen, D.S., et al. (2014). Measurement of a doubly substituted methane isotopologue, $^{13}CH_3D$, by tunable infrared laser direct absorption spectroscopy. *Analytical Chemistry, 86*, 6487-6494. doi:10.1021/ac5010579

Pape, T., Hohnberg, H.J., Wunsch, D., et al. (2017). Design and deployment of autoclave pressure vessels for the portable deep-sea drill rig MeBo (Meeresboden-Bohrgerät). *Scientific Drilling*, 23, 29-37. doi:10.5194/sd-23-29-2017

Pepper, A.S., & Corvi, P.J. (1995). Simple kinetic models of petroleum formation. Part I: oil and gas generation from kerogen. *Marine and Petroleum Geology*, 12, 291-319. doi:10.1016/0264-8172(95)98381-E

Peng, T.R., Wang, C.H., Huang, C.C., et al. (2010). Stable isotopic characteristic of Taiwan's precipitation: A case study of western Pacific monsoon region. *Earth and Planetary Science Letters,* 289, 357-366. doi:10.1016/j.epsl.2009.11.024

Poreda, R., & Craig, H. (1989). Helium isotope ratios in circum-Pacific volcanic arcs. *Nature,* 338, 473-478. doi:10.1038/338473a0

Rau, R.J., Lee, J.C., Ching, K.E., et al. (2012). Subduction-continent collision in southwestern Taiwan and the 2010 Jiashian earthquake sequence. *Tectonophysics*, 578, 107-116. doi:10.1016/j.tecto.2011.09.013

Roulleau, E., Sano, Y., Takahata, N., et al. (2015). He, Ar, N and C isotope compositions in Tatun Volcanic Group (TVG), Taiwan: Evidence for an important contribution of pelagic carbonates in the magmatic source. *Journal of Volcanology and Geothermal Research*, 303, 7-15. doi:0.1016/j.jvolgeores.2015.07.017

Rumble, D., Ash, J.L., Wang, P.L., et al. (2018). Resolved measurements of $^{13}CDH_3$ and $^{12}CD_2H_2$ from a mud volcano in Taiwan. *Journal of Asian Earth Sciences,* 167, 218-221. doi:10.1016/j.jseaes.2018.03.007

Sano, Y., Kinoshita, N., Kagoshima, T., et al. (2017). Origin of methane-rich natural gas at the West Pacific convergent plate boundary. *Scientific reports,* 7, 1-10. doi:10.1038/s41598-017-15959-5

Sano, Y., Tokutake, T., & Takahata, N. (2008). Accurate measurement of atmospheric helium isotopes. *Analytical sciences: The international journal of the Japan Society for Analytical Chemistry,* 24, 521-525. doi:10.2116/analsci.24.521

Schoell, M. (1988). Multiple origins of methane in the Earth. *Chemical Geology,* 71, 1-10. doi:10.1016/0009-2541(88)90101-5

Scholten, J.C., & Conrad, R. (2000). Energetics of syntrophic propionate oxidation in defined batch and chemostat cocultures. *Applied and Environmental Microbiology*, 66, 2934-2942. doi:10.1128/AEM.66.7.2934-2942.2000

Shao, W.Y., Chung, S.L., & Chen, W.S. (2014). Zircon U-Pb Age Determination of Volcanic Eruptions in Lutao and Lanyu in the Northern Luzon Magmatic Arc. Terrestrial, *Atmospheric and Oceanic Sciences*, 25, 149. doi:10.3319/TAO.2013.11.06.01(TT)

Shuai, Y., Douglas, P.M., Zhang, S., et al. (2018). Equilibrium and non-equilibrium controls on the abundances of clumped isotopologues of methane during thermogenic formation in laboratory experiments: implications for the chemistry

of pyrolysis and the origins of natural gases. *Geochimica et Cosmochimica Acta,* 223, 159-174. doi:10.1016/j.gca.2017.11.024

Stolper, D.A., Lawson, M., Davis, C.L., et al. (2014). Formation temperatures of thermogenic and biogenic methane. *Science*, 344, 1500-1503, doi: 10.1126/science.1254509

Stolper, D.A., Martini, A.M., Clog, M., et al. (2015). Distinguishing and understanding thermogenic and biogenic sources of methane using multiply substituted isotopologues. *Geochimica et Cosmochimica Acta*, 161, 219-247. doi:10.1016/j.gca.2015.04.015

Summons, R.E., Franzmann, P.D., & Nichols, P.D. (1998). Carbon isotopic fractionation associated with methylotrophic methanogenesis. *Organic Geochemistry*, 28, 465-475. doi:10.1016/S0146-6380(98)00011-4

Sun, C.H., Chang, S.C., Kuo, C.L., et al. (2010). Origins of Taiwan's mud volcanoes: Evidence from geochemistry. *Journal of Asian Earth Sciences,* 37, 105-116. doi:10.1016/j.jseaes.2009.02.007

Suppe, J. (1984). Kinematics of arc-continent collision, flipping of subduction, and back-arc spreading near Taiwan. *Geological Society of China Memoir,* 6, 131-146

Takai, K., Nakamura, K., Toki, T., et al. (2008). Cell proliferation at 122oC and isotopically heavy CH4 production by a hyperthermophilic methanogen under high-pressure cultivation. *Proceedings of the National Academy of Sciences*, 105, 10949-10954. doi:10.1073/pnas.0712334105

Teng, L.S., & Lin, A.T. (2004). Cenozoic tectonics of the China continental margin: Insights from Taiwan. *Geological Society, London, Special Publications,* 226, 313-332. doi:10.1144/gsl.Sp.2004.226.01.17

Tseng, Y., Römer, M., Lin, S., et al. (2023). Yam Seep at Four-Way Closure Ridge: a prominent active gas seep system at the accretionary wedge SW offshore Taiwan. *International Journal of Earth Sciences*, 112, 1043-1061. doi:10.1007/s00531-022-02280-4

Warr, O., Young, E. D., Giunta, T., et al. (2021). High-resolution, long-term isotopic and isotopologue variation identifies the sources and sinks of methane in a deep subsurface carbon cycle. *Geochimica et Cosmochimica Acta*, 294, 315-334. doi:10.1016/j.gca.2020.12.002

Wang, D.T., Gruen, D.S., Lollar, B.S., et al. (2015). Nonequilibrium clumped isotope

signals in microbial methane. *Science,* 348, 428. doi:10.1126/science.aaa4326

Wang, P.-L., Wu, J.-J., Yeh, E.-C., et al. (2010) Isotopic constraints of vein carbonates on fluid sources and processes associated with the ongoing brittle deformation within the accretionary wedge of Taiwan. *Terra Nova*, 22, 251–256. doi: 10.1111/j.1365-3121.2010.00940.x

Wang, P.L., Chiu, Y.P., Cheng, T.W., et al. (2014). Spatial variations of community structures and methane cycling across a transect of Lei-Gong-Hou mud volcanoes in eastern Taiwan. *Frontiers in Microbiology*, 5, 121. doi:10.3389/fmicb.2014.001

Wang, Y., Lin, Y.N., Ota, Y., et al. (2022). Mud Diapir or Fault-Related Fold? On the Development of an Active Mud-Cored Anticline Offshore Southwestern Taiwan. *Tectonics*, 41, e2022TC007234. doi:10.1029/2022TC007234

Whiticar, M.J. (1999). Carbon and hydrogen isotope systematics of bacterial formation and oxidation of methane. *Chemical Geology*, 161, 291-314. doi:10.1016/S0009-2541(99)00092-3

Xia, X., & Gao, Y. (2019). Kinetic clumped isotope fractionation during the thermal generation and hydrogen exchange of methane. *Geochimica et Cosmochimica Acta*, 248, 252-273. doi:10.1016/j.gca.2019.01.004

Xia, X., & Gao, Y. (2021). Methane from microbial hydrogenolysis of sediment organic matter before the great oxidation event. *Nature communications*, 12, 5032. doi:10.1038/s41467-021-25336-6

Yang, T.F., Chen, C.H., Tien, R.L., et al. (2003). Remnant magmatic activity in the Coastal Range of East Taiwan after arc–continent collision: fission-track data and $^{3}He/^{4}He$ ratio evidence. *Radiation Measurements,* 36, 343-349. doi:10.1016/S1350-4487(03)00149-5

Yang, T.F., Yeh, G.H., Fu, C.C., et al. (2004). Composition and exhalation flux of gases from mud volcanoes in Taiwan. *Environmental Geology*, 46, 1003-1011. doi:10.1007/s00254-004-1086-0

Yeh, Y.L., Strong, W., Chien W.C., et al. (2016). Tomography of the Chukou Fault zone, southwest Taiwan: Insights from microearthquake data. *TAO: Terrestrial, Atmospheric and Oceanic Sciences,* 27, 387. doi:10.3319/TAO.2016.01.29.01

Yen, J.Y., Chen, K.S., Chang, C.P., et al. (2008). Evaluation of earthquake potential and surface deformation by differential interferometry. *Remote Sensing of Environment*, 112, 782-795. doi:10.1016/j.rse.2007.06.012

Yeung, L.Y., Li, S., Kohl, I.E., et al. (2017). Extreme enrichment in atmospheric $^{15}N^{15}N$. *Science Advances*, 3, 6741. doi:10.1016/j.chemgeo.2022.120709

You, C.F., Gieskes, J. M., Lee, T., et al. (2004). Geochemistry of mud volcano fluids in the Taiwan accretionary prism. *Applied Geochemistry,* 19, 695-707. doi:10.1016/j.apgeochem.2003.10.004

Young, E.D., Kohl, I.E., Lollar, B.S., et al. (2017). The relative abundances of resolved $^{l2}CH_2D_2$ and $^{13}CH_3D$ and mechanisms controlling isotopic bond ordering in abiotic and biotic methane gases. *Geochimica et Cosmochimica Acta,* 203, 235-264. doi:10.1016/j.gca.2016.12.041

Young, E.D., Rumble, D., Freedman, P., et al. (2016). A large-radius high-mass-resolution multiple-collector isotope ratio mass spectrometer for analysis of rare isotopologues of O_2, N_2, CH_4 and other gases. *International Journal of Mass Spectrometry*, 401, 1-10. doi:10.1016/j.ijms.2016.01.006

Yu, H.S., & Chang, E. T. Y. (2009). Links among slope morphology, canyon types and tectonics on passive and active margins in the northernmost South China Sea. *Journal of Earth Science*, 20, 77-84. doi:10.1007/s12583-009-0008

Figure captions

Figure 1. Isotopic and abundance characteristics of hydrocarbons and CO_2 for analyzed samples. (a) $\delta^{13}C_{CH4}$ versus $\delta^{2}H_{CH4}$ values (data from Table S2); (b) $C_1/ (C_2+C_3)$ ratios versus $\delta^{13}C_{CH4}$ values (data from Table S1); (c) $\delta^{13}C_{CO2}$ versus $\delta^{13}C_{CH4}$ values (data from Table S1). The plotted fields are divided into areas for “primary microbial” (shaded in green and blue), “secondary microbial” (encircled by dashed lines and abbreviated as “SM”), “thermogenic” (shaded in yellow), and “abiotic” (shaded in orange) formation processes following the ranges of Milkov and Etiope (2018). “Primary microbial” methane is further divided into two categories, with “F” for the fermentation of methylated compounds, and “CR” for the CO_2 reduction. Results are categorized by structural domains (yellow squares – Chukou Fault, green circles – Chishan Fault, crosses – Guitingkeng Anticline, light yellow circles – Coastal Plain, blue squares – offshore FR and FWCR sites, orange triangles – Coastal Range). Green and black arrows in (a) and (b) show the possible trends for microbial methane oxidation and diffusion of migratory methane, respectively. The slope

of the arrow does not indicate the precise variation trend. Some published results for different processes simultaneously characterized by the abundances of doubly substituted isotopologues (Young et al., 2017; Giunta et al., 2019) are plotted for comparison.

Figure 2. $\Delta^{12}CH_2D_2$ versus $\Delta^{13}CH_3D$ values for analyzed samples. The equilibrium curve marked with temperature was calculated following Young et al. (2016). Sample legends are the same as those in Figure 1. Values for microbial methane produced from methylated compounds and from CO_2 in the lab (blue diamonds encompassed with an arbitrarily defined range in green and gray; Young et al., 2017 and Giunta et al., 2019), abiotic methane produced in the laboratory (orange diamonds) or recovered from the field (gray circles with cross marks) (Young et al., 2017) are plotted for comparison. Green, black, and blue arrows show the possible trends for aerobic oxidation of methane, diffusion of migratory methane, and anaerobic oxidation of methane (AOM), respectively. The slope of the arrow does not indicate the precise variation trend. Data distribution within the region encircled by a dashed rectangle is enlarged in the lower right corner.

Figure 3. $^{20}Ne/^{4}He$ versus $^{3}He/^{4}He$ ratios (in Ra) for analyzed samples. A three end-component mixing model encompasses “crust”, “mantle”, and “air” components with He isotope ratios of 0.01, 8, and 1 Ra, respectively (Poreda & Craig, 1989). Legends are the same as those in Figure 1.

Figure 4. Water isotopic compositions and fractionations, and methane isotopologue abundances. (a) Water $\delta^{2}H$ versus $\delta^{18}O$ values for analyzed samples. Legends are the same as those in Figure 1 (except for the red star for seawater from the Green Island; small blue circles for meteoric water in eastern and southern Taiwan). The solid line indicates the global meteoric water line (GMWL; Craig, 1961), whereas the dashed line is the local meteoric water line (LMWL; Peng et al., 2010). The dotted lines with arrows indicate the potential mixing between deeply sourced water and meteoric water or seawater. Data for mud volcanoes published in previous studies are also plotted for comparison. (b) $\Delta^{13}CH_3D$ and (c) $\Delta^{12}CH_2D_2$ values versus hydrogen isotopic fractionations (ε; defined as $(\alpha-1)\times1000‰$, where α is the fractionation factor (eq. 8) between methane and water). The equilibrium curves (in blue dashed lines) are plotted using the relationships described in Horita & Wesolowski (1994) and Horibe & Craig

(1995). The dotted lines indicate an infinite temperature that is based on two methane isotopologue abundances (Young et al., 2016).

Figure 5. Schematic geological cross sections (modified from Chen (2016)) overlaid with the estimated depths of methane formation (solid orange circles) based on methane isotopologue abundances (this study) and local geothermal gradients (Chi & Reed, 2008) (Table S6). The geographic distribution of each cross section is excerpted from the solid lines in Figure 5d. Faults with the shearing sense related to individual structural domains were shown in black dashed lines with arrows. The estimated depths of methane formation are projected directly on the related faults to help visualize the possible two-dimensional range where methane is formed. Therefore, it is likely that the exact positions of methane formation deviate from the attributed fault systems (e.g., blind faults). Interpretations for the origins of methane and helium are also provided in parentheses next to site names with the first letter denoting for methane (T for thermogenic, B for biogenic, and A for abiotic) and the second letter for helium (C for crust and M for mantle). Although the temperature (and depth) estimate (~190°C) based on two methane isotopologue abundances for site WD is available, no schematic cross section has been published due to the lack of subsurface geology data.

Figure 1.

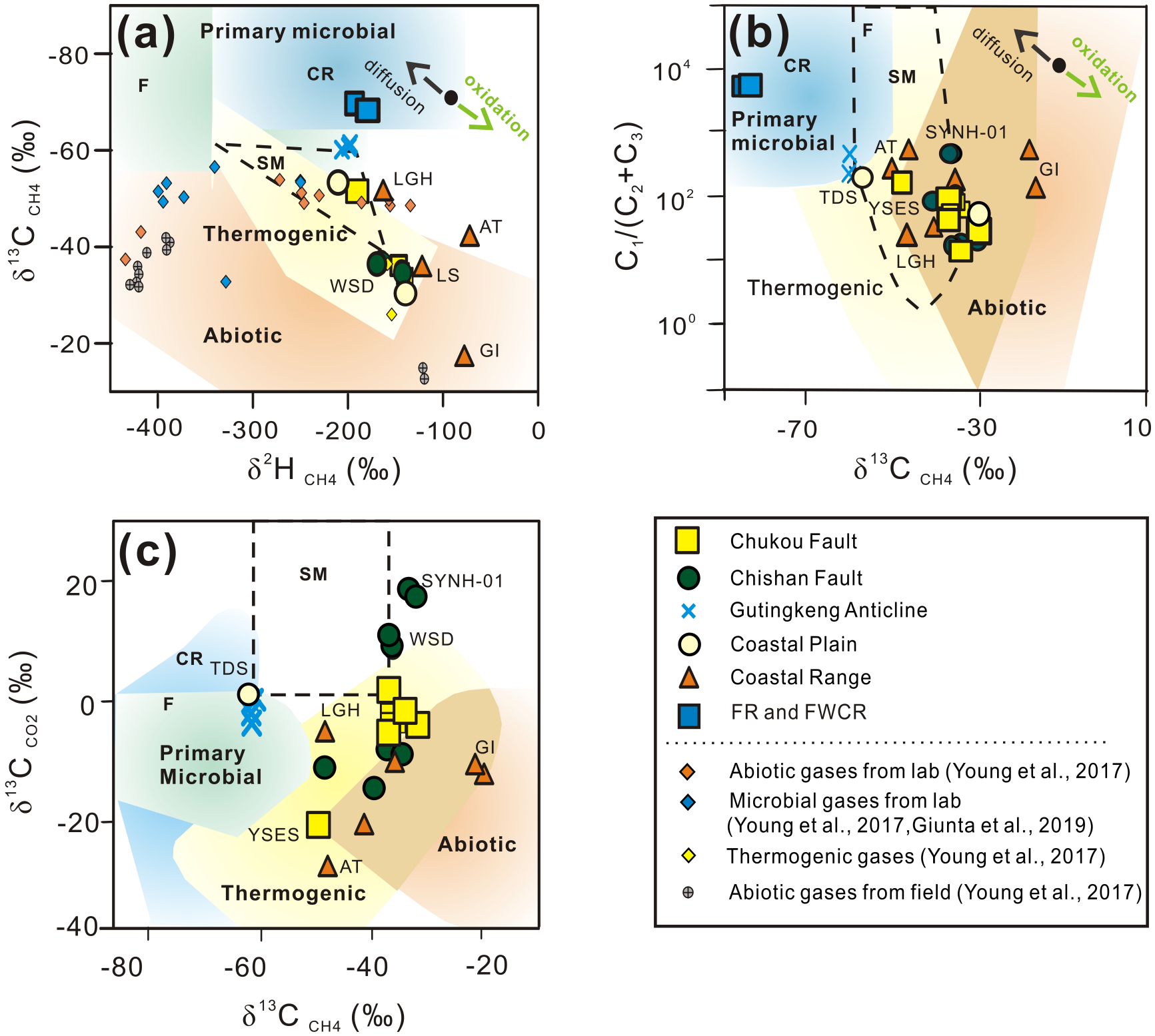
(a)
Primary microbial
CR
diffusion
oxidation
F
SM
LGH
Thermogenic
AT
WSD
LS
Abiotic
GI
-80
-60
-40
-20
-400
-300
-200
-100
0
δ13C CH4 (‰)
δ2H CH4 (‰)
(b)
F
CR
SM
diffusion
oxidation
Primary microbial
SYNH-01
AT
GI
TDS
YSES
LGH
Thermogenic
Abiotic
10^4
10^2
10^0
-70
-30
10
C1/(C2+C3)
δ13C CH4 (‰)
(c)
SM
SYNH-01
WSD
CR
TDS
F
LGH
GI
Primary Microbial
YSES
Abiotic
AT
Thermogenic
20
0
-20
-40
-80
-60
-40
-20
δ13C CO2 (‰)
δ13C CH4 (‰)
Chukou Fault
Chishan Fault
Gutingkeng Anticline
Coastal Plain
Coastal Range
FR and FWCR
Abiotic gases from lab (Young et al., 2017)
Microbial gases from lab
(Young et al., 2017,Giunta et al., 2019)
Thermogenic gases (Young et al., 2017)
Abiotic gases from field (Young et al., 2017)

Figure 2.

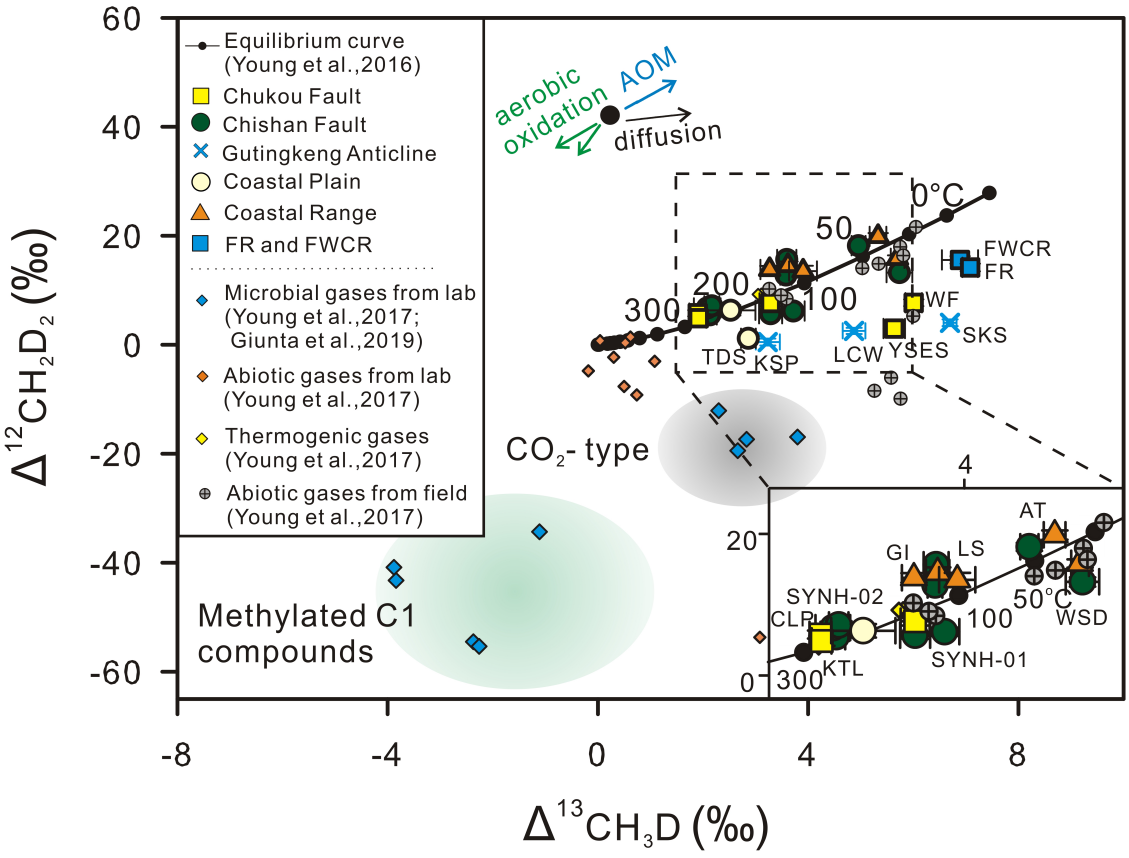
Equilibrium curve
(Young et al.,2016)
Chukou Fault
Chishan Fault
Gutingkeng Anticline
Coastal Plain
Coastal Range
FR and FWCR
Microbial gases from lab
(Young et al.,2017;
Giunta et al.,2019)
Abiotic gases from lab
(Young et al.,2017)
Thermogenic gases
(Young et al.,2017)
Abiotic gases from field
(Young et al.,2017)
aerobic oxidation
AOM
diffusion
0°C
50
100
200
300
FWCR
FR
WF
SKS
LCW
YSES
TDS
KSP
CO2- type
Methylated C1
compounds
4
20
0
AT
GI
LS
SYNH-02
CLR
50°C
100
WSD
SYNH-01
300
KTL
60
40
20
0
-20
-40
-60
-8
-4
0
4
8
Δ12CH2D2 (‰)
Δ13CH3D (‰)

Figure 3.

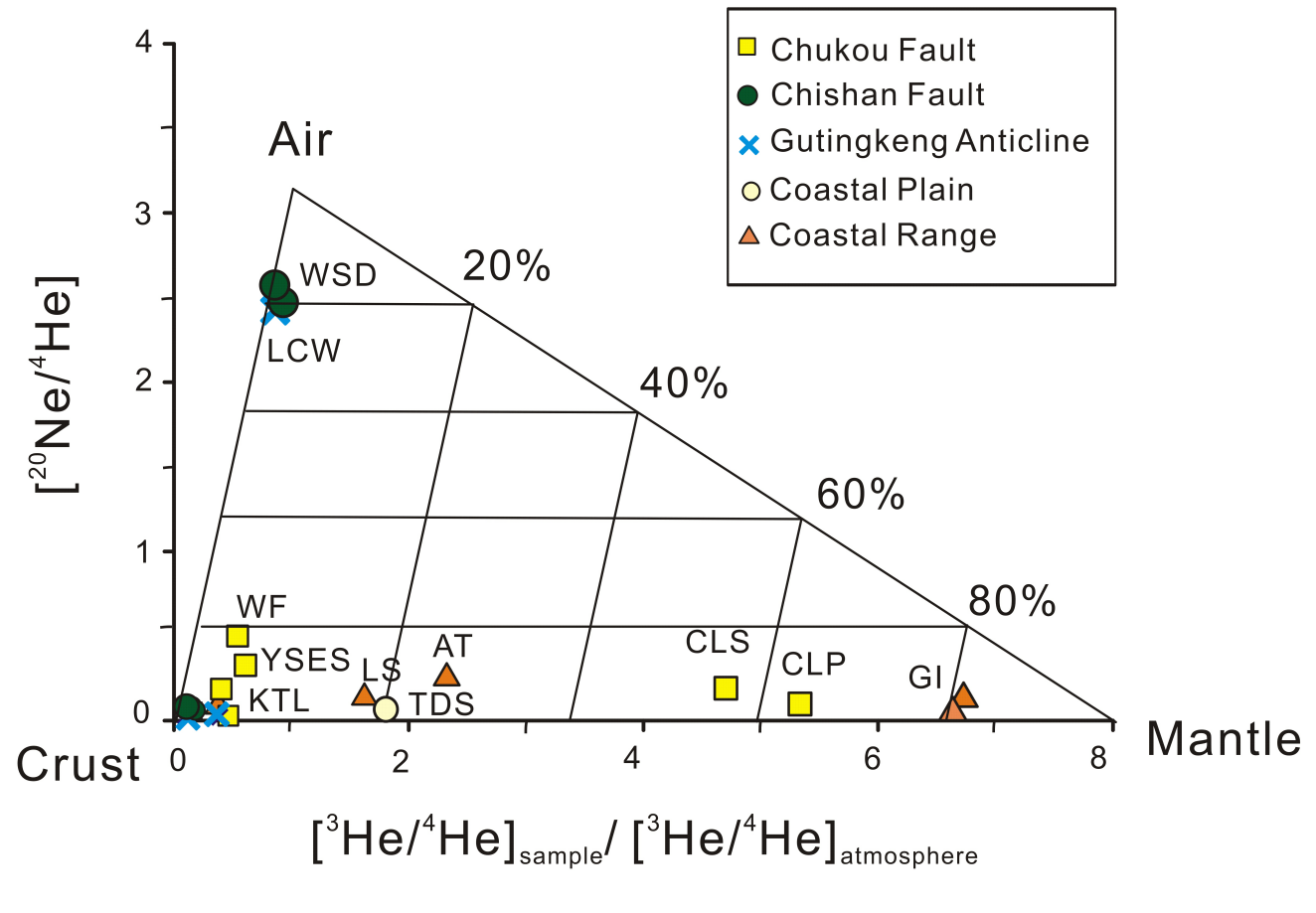
Chukou Fault
Chishan Fault
Gutingkeng Anticline
Coastal Plain
Coastal Range
Air
20%
40%
60%
80%
WSD
LCW
WF
YSES
KTL
LS
AT
TDS
CLS
CLP
GI
Crust
Mantle
0
1
2
3
4
0
2
4
6
8
[20Ne/4He]
[3He/4He]sample/ [3He/4He]atmosphere

Figure 4.

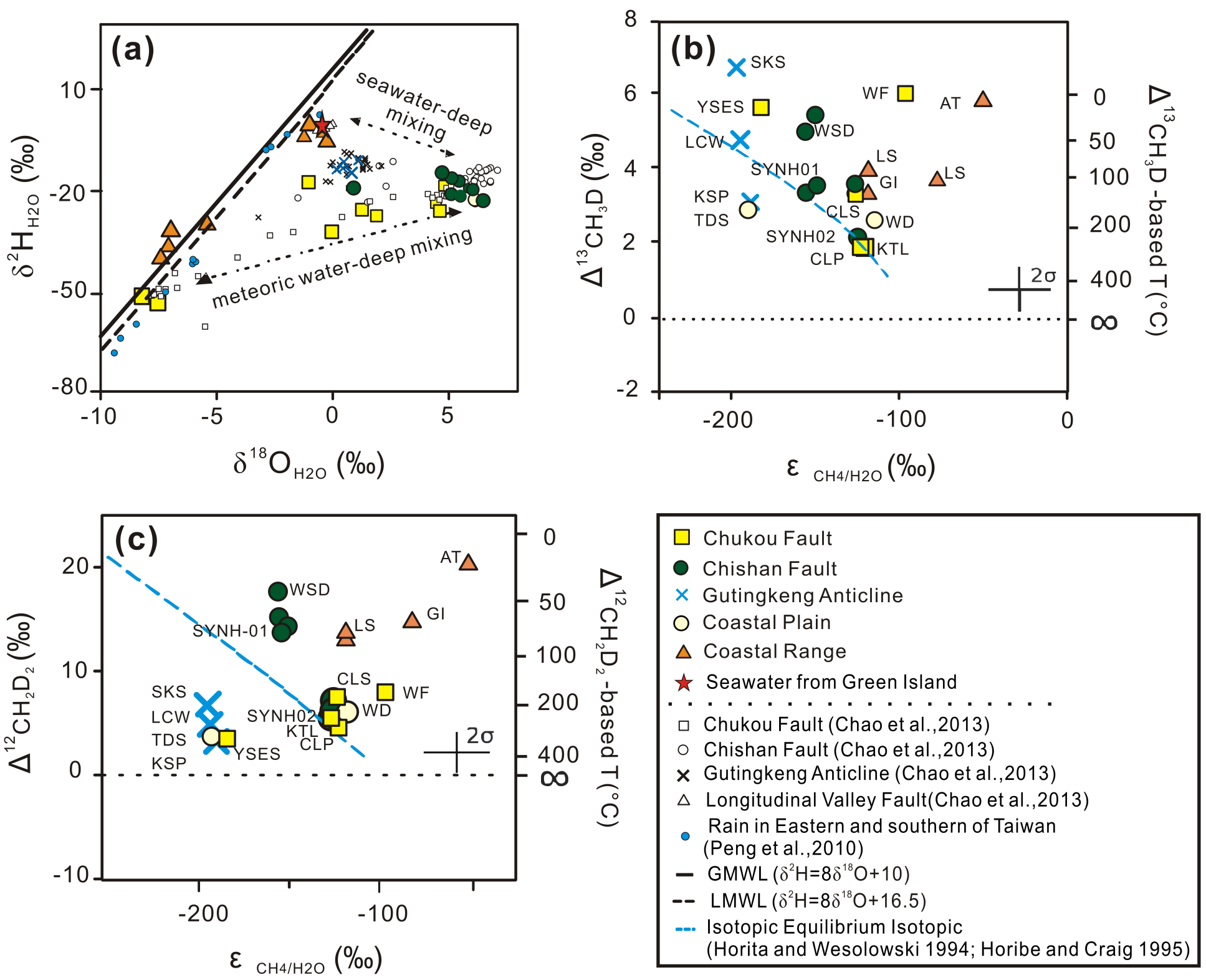
(a)
seawater-deep mixing
meteoric water-deep mixing
δ2HH2O (‰)
δ18OH2O (‰)
(b)
SKS
YSES
LCW
KSP
TDS
WF
AT
WSD
LS
SYNH01
GI
CLS
WD
SYNH02
KTL
CLP
2σ
Δ13CH3D (‰)
ε CH4/H2O (‰)
Δ13CH3D -based T (°C)
(c)
AT
WSD
SYNH-01
LS
GI
CLS
WF
SKS
LCW
TDS
KSP
SYNH02
KTL
CLP
WD
YSES
2σ
Δ12CH2D2 (‰)
ε CH4/H2O (‰)
Δ12CH2D2 -based T (°C)
Chukou Fault
Chishan Fault
Gutingkeng Anticline
Coastal Plain
Coastal Range
Seawater from Green Island
Chukou Fault (Chao et al.,2013)
Chishan Fault (Chao et al.,2013)
Gutingkeng Anticline (Chao et al.,2013)
Longitudinal Valley Fault(Chao et al.,2013)
Rain in Eastern and southern of Taiwan (Peng et al.,2010)
GMWL (δ2H=8δ18O+10)
LMWL (δ2H=8δ18O+16.5)
Isotopic Equilibrium Isotopic (Horita and Wesolowski 1994; Horibe and Craig 1995)

Figure 5.

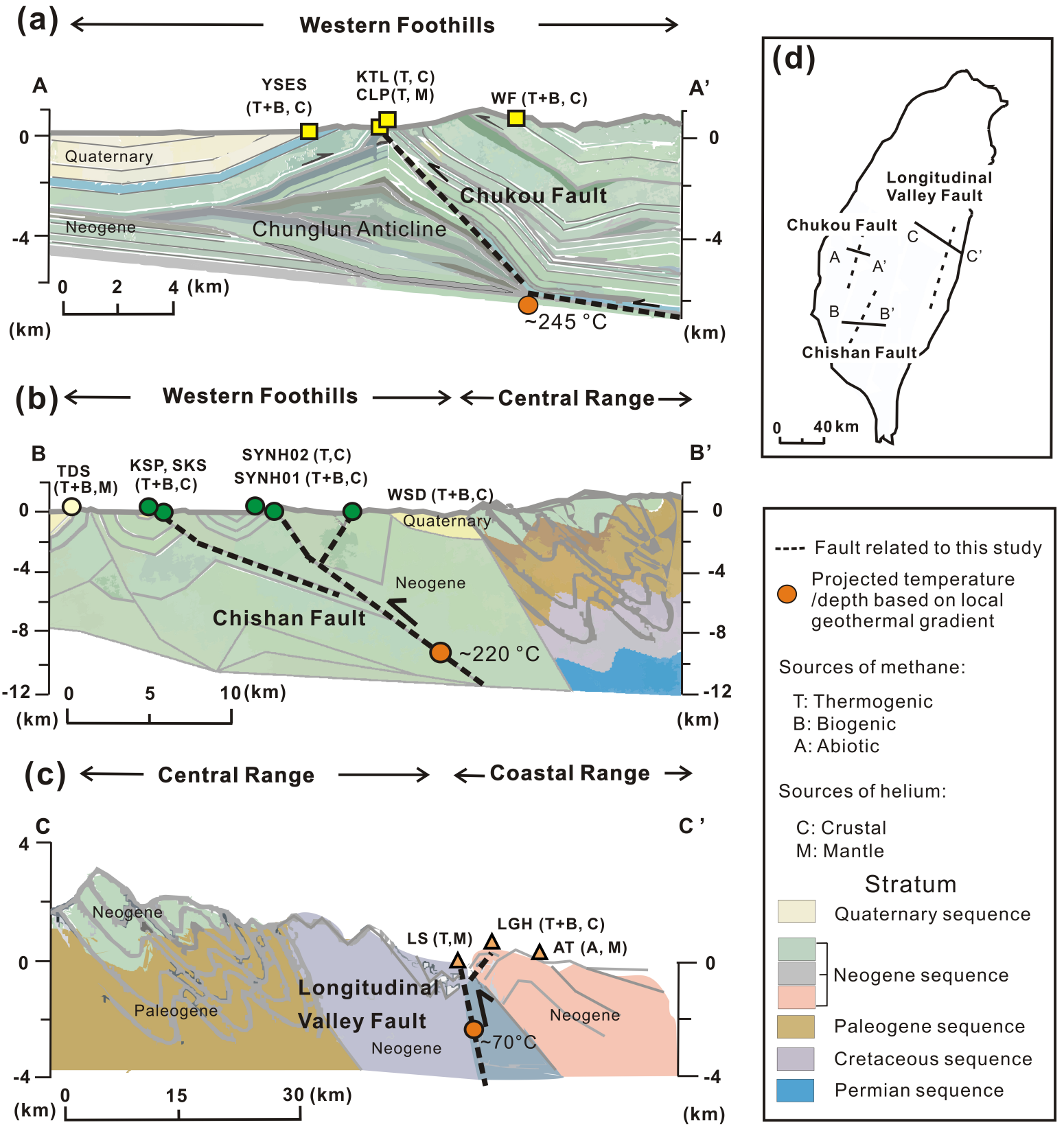
(a)
Western Foothills
A
A'
YSES
(T+B, C)
KTL (T, C)
CLP(T, M)
WF (T+B, C)
Quaternary
Neogene
Chunglun Anticline
Chukou Fault
~245 °C
0
-4
0
2
4 (km)
(km)
(km)
(b)
Western Foothills
Central Range
B
B'
TDS
(T+B,M)
KSP, SKS
(T+B,C)
SYNH02 (T,C)
SYNH01 (T+B,C)
WSD (T+B,C)
Quaternary
Neogene
Chishan Fault
~220 °C
0
-4
-8
-12
0
5
10 (km)
(km)
(km)
(c)
Central Range
Coastal Range
C
C'
Neogene
Paleogene
LS (T,M)
LGH (T+B, C)
AT (A, M)
Longitudinal
Valley Fault
Neogene
Neogene
~70°C
4
0
-4
0
15
30 (km)
(km)
(km)
(d)
Longitudinal
Valley Fault
Chukou Fault
A
A'
B
B'
C
C'
Chishan Fault
0
40 km
---- Fault related to this study
Projected temperature /depth based on local geothermal gradient
Sources of methane:
T: Thermogenic
B: Biogenic
A: Abiotic
Sources of helium:
C: Crustal
M: Mantle
Stratum
Quaternary sequence
Neogene sequence
Paleogene sequence
Cretaceous sequence
Permian sequence